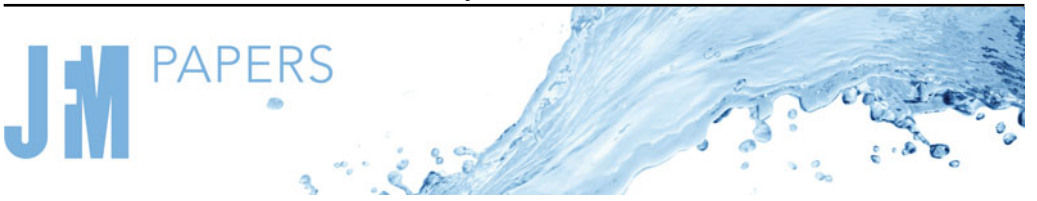
J. Fluid Mech. (2026), *vol.* 1042, A37, doi:10.1017/jfm.2026.11990



Bubble detachment from solid surfaces induced by impacting particles

Xin Chen[1], **Li Xin**[1], **Bifeng Yin**[1], **Ying Zhang**[1], **Jie Ni**[1] **and Fei Dong**[1]

[1]School of Automotive and Traffic Engineering, Jiangsu University, 301 Xuefu Road, Zhenjiang 212013, PR China

Corresponding author: Fei Dong, jsdxdf@163.com

(Received 20 April 2025 UTC; revised 24 June 2026 UTC; accepted 28 July 2026 UTC)

In this paper, the coupled volume-of-fluid and level set method, immersed boundary method and discrete element method is extended to an axisymmetric configuration to investigate bubble detachment from solid surfaces induced by particle impact. The post-impact dynamics is systematically investigated over a range of Weber numbers (We), particle wettabilities (θ_p), density ratios (k_ρ) and size ratios (k_r). The results reveal three distinct detachment modes: capillary-wave detachment (CWD), bubble-rebound detachment (BRD) and particle-rebound detachment (PRD). At low We, early spreading over the particle releases surface energy and excites capillary waves that drive contact-line motion and rapid detachment. The spreading follows a power law, with the exponent increasing with We, reflecting the increasing contribution of impact inertia to the spreading process. As We increases, inertial compression suppresses capillary-wave-induced momentum reversal and the detachment mode shifts to BRD, where momentum reversal is achieved through the release of stored deformation energy. At sufficiently high We, particle rebound from the substrate injects a strong upward momentum into the flow, leading to PRD. Kelvin impulse analysis is employed to quantify the evolution of vertical momentum and establish a unified interpretation of the detachment process. A detachment capability factor is further proposed to characterise the competition between interfacial energy release and inertial suppression. Regime maps in the (We, θ_p), (We, k_ρ) and (We, k_r) parameter spaces are constructed, demonstrating that mode transitions are governed by the balance between capillary-wave-driven momentum generation and inertia-induced suppression.

Key words: bubble dynamics, contact lines, particle/fluid flows

https://doi.org/10.1017/jfm.2026.11990 Published online by Cambridge University Press

© The Author(s), 2026. Published by Cambridge University Press.

1. Introduction

The collision between particles and dispersed fluid–fluid interfaces (including bubbles and droplets) is commonly encountered in various industrial processes such as spraying (Gong, Li & Kang 2022; Zhang *et al.* 2023), flotation (Hassanzadeh *et al.* 2018; Han *et al.* 2022), catalytic reactions (Chen *et al.* 2023) and liquid cooling (Chen *et al.* 2025*b*). During collisions, the influence of particles can cause behaviours such as spreading, rebound and breakup of drops. These behaviours significantly affect industrial processes, such as altering heat transfer performance (Fardan, Berndt & Ahmed 2021) and the active surface area of catalytic particles (Ge & Fan 2007). Therefore, investigating the dynamic behaviour of collisions is crucial for optimising these processes.

Dispersed fluid–fluid interfaces mainly exist in the form of droplets or bubbles. The particle–droplet collision problem can be categorised into three scenarios based on the initial conditions: droplets impacting stationary particles, particles impacting stationary droplets and the collision of moving particles and moving droplets. There has been extensive research on the impact of droplets on particle surfaces (Pawar *et al.* 2016; Janssen *et al.* 2023). After impact, droplets undergo three stages: the initial droplet deformation, an inertia-control stage and a viscous dominance stage (Mitra *et al.* 2017). The governing factors of these processes can be characterised by two dimensionless parameters, namely the Weber number (We) and Reynolds number (Re) (Yoon & Shin 2021). Additionally, the surface characteristics of the particles are key factors affecting impact behaviour. Under varying impact conditions, droplets may exhibit different phenomena such as spreading, rebound, breakup and splashing (Wu *et al.* 2022). In the case of particles impacting droplets, two behaviours can be observed depending on the impact conditions: partial submersion and complete submersion (penetration) (Mitra *et al.* 2015). During the impact process, particles are primarily influenced by gravity and capillary forces. If the particle velocity has decreased to zero before complete submersion, this is considered partial submersion. Otherwise, the particle will penetrate the droplet. When suspended particles collide with suspended droplets, four behaviours can occur: agglomeration, separation, penetration and breakage (Singh & Joseph 2005; Deen, Annaland & Kuipers 2009). Although significant research has been conducted on particle–droplet collision phenomena, many findings do not universally apply to all scaling laws (Cheng, Sun & Gordillo 2021). Numerous fundamental questions remain to be explored further.

Bubbles in a second-phase fluid typically exist in two forms due to the significant buoyancy forces acting on them: suspended within the fluid and attached to a solid wall (Brabcová *et al.* 2015; Mohammadi *et al.* 2022). Current research on particle–bubble interaction primarily focuses on flotation processes. The success of particle flotation hinges on two core aspects (Wang *et al.* 2025): first, the rupture of the hydration film between the particle and the bubble, which forms a three-phase contact line; second, the external forces acting on the particle must be less than the forces between the particle and the bubble, preventing the particle from detaching from the bubble surface. The flotation process is mainly influenced by factors such as particle size, wettability and the relative velocity between particles and bubbles. It is evident that the flotation process emphasises the movement of particles on the bubble surface, with less attention paid to bubble behaviour.

In boiling processes, the nucleation, growth and detachment of bubbles on heated surfaces have a decisive impact on boiling heat transfer performance (Bureš & Sato 2022; Chen *et al.* 2024; Park *et al.* 2024). When fluid media contain particles, complex interactions occur between the particles and bubbles (Hsu *et al.* 2024). Iwata *et al.* (2010) and Washino *et al.* (2023) studied the rising behaviour of bubbles in sparse

https://doi.org/10.1017/jfm.2026.11990 Published online by Cambridge University Press

spherical particle clusters and irregular particle clusters, respectively. Yu *et al.* (2024) investigated the rising behaviour of bubbles in dense particle beds. However, these studies did not address the effect of particles on bubble detachment from heated surfaces. In our previous study (Chen *et al.* 2025*a*), we investigated the wetting dynamics of a bubble lying between a free particle and a solid horizontal surface. The particle was initially at rest, and the interaction was governed predominantly by capillary effects. Upon contact, capillary waves were generated and propagated along the vapour–liquid interface, driving the motion of the three-phase contact line and eventually inducing bubble detachment from the solid surface. The important role of capillary waves in interfacial transport has also been demonstrated in other multi-phase systems. Huang *et al.* (2026) recently demonstrated centimetre-scale droplet jumping on superhydrophobic surfaces induced by capillary waves generated during entrained bubble bursting.

However, in practical particulate boiling systems and vapour–liquid–solid three-phase flows, particles typically collide with bubbles at finite velocities. Under such conditions, particle inertia acts together with capillary forces, giving rise to interfacial dynamics that differs from that arising solely from capillary effects. When particles collide with bubbles on a heated surface, phenomena similar to particles impacting droplets can be observed, where particles may become attached to the bubble surface or submerge within the bubble (Yang *et al.* 2023). Meanwhile, the bubble may undergo compression, rebound, interfacial-wave propagation or even transitions between different detachment modes, thereby altering the local flow structure and affecting local heat and mass transfer processes (Rahmati *et al.* 2020). Therefore, a systematic investigation of particle-impact-induced bubble detachment is required to elucidate the underlying interfacial dynamics and detachment mechanisms.

To the best of our knowledge, the dynamical mechanisms by which a solid particle impacts a wall-adhered bubble and induces its detachment have not yet been systematically explored. Unlike our previous studies that focused on capillary-driven wetting processes involving a particle initially at rest (Chen *et al.* 2025*a*), the present work investigates impact-induced detachment of wall-adhered bubbles under the combined action of particle inertia and capillary effects. Furthermore, the present study considers an axisymmetric particle–bubble system, enabling a more realistic representation of impact-induced bubble deformation and detachment than the two-dimensional planar configuration considered previously. To address this problem, the three-phase flow model based on the coupled volume-of-fluid and level set method, immersed boundary method and discrete element method (VOSET-IBM-DEM) is extended to an axisymmetric framework and employed to numerically investigate the post-impact evolution of a single particle–bubble system, with particular focus on bubble detachment. By incorporating the Kelvin impulse framework together with an energy-based analysis, we identify distinct bubble-detachment regimes and examine how particle properties (including wettability, density ratio and size ratio) affect the detachment behaviour over a range of Weber numbers. The dependence of detachment time and regime transition on the governing physical parameters is elucidated, and the underlying mechanisms are interpreted in terms of interfacial energy release and momentum evolution.

2. Problem statement

We conduct numerical simulations to investigate the dynamics of a particle impacting a bubble attached to a solid wall under an axisymmetric framework. In practical situations, bubbles deform into an ellipsoidal shape due to buoyancy force. To realistically reproduce the bubble morphology, a preliminary simulation of a vapour–liquid two-phase flow without a particle is first performed. The computational configuration for the bubble

https://doi.org/10.1017/jfm.2026.11990 Published online by Cambridge University Press

Medium	Liquid	Vapour
Density (kg m^{-3})	958	0.6
Dynamic viscosity (Pa s)	2.82×10^{-4}	1.23×10^{-5}
Surface tension coefficient (N m^{-1})	0.059	

Table 1. Physical properties of water (liquid and vapour).

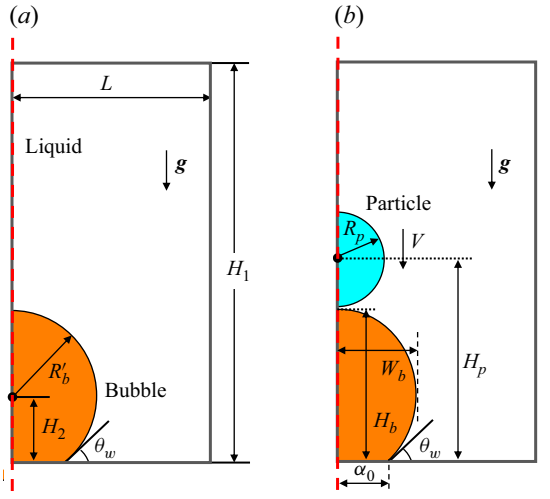


Figure 1. Schematic of the computational configuration: (*a*) pre-simulation stage for establishing the equilibrium shape of the surface-attached bubble and (*b*) particle–bubble impact stage after introducing the particle.

pre-simulation is shown in figure 1(*a*). The equivalent bubble diameter is set to $D_b = 1.5$ mm, and the contact angle at the bottom wall is fixed at $\theta_w = 45°$. The initial vertical distance between the bubble centre and the bottom wall, H_2, as well as the effective bubble radius R'_b, are determined based on the bubble diameter D_b and the wall contact angle θ_w. The computational domain has dimensions of $L = 1.5D_b$ in the horizontal direction and $H_1 = 3D_b$ in the vertical direction.

After the bubble reaches a stable configuration, a particle is introduced above the bubble with an initial downward velocity V. The particle diameter is denoted as D_p, and the detailed configuration is illustrated in figure 1(*b*). The bubble diameter D_b and the particle impact velocity V are chosen as the characteristic length scale and characteristic velocity, respectively.

Deionised water is selected as the working fluid in this study. The physical properties of the liquid and vapour phases correspond to those at the saturation condition under atmospheric pressure and are listed in table 1. The particle contact angle is denoted by θ_p, and the density of the particles is referred to as ρ_s. The density ratio between the particles and the liquid phase is defined as $k_\rho = \rho_s/\rho_l$, and the size ratio between the particles and the bubble is defined as $k_r = D_p/D_b$.

In the boiling of deionised water at low superheating, the entire cycle from nucleation to growth of bubbles spans several tens to hundreds of milliseconds (Siegel & Keshock 1964; Kunkelmann 2011; Ling, Li & Tao 2014). The results of this study indicate that the entire

https://doi.org/10.1017/jfm.2026.11990 Published online by Cambridge University Press

process of bubble detachment following particle impact occurs within 20 ms. Therefore, the effect of bubble growth is not considered in this study.

3. Numerical methods

The collision process of a particle into a bubble is simulated using the VOSET-IBM-DEM developed by our group (Chen, Yin & Dong 2024*a*,*b*). This method is based on the finite-volume method, which solves for the fluid and particles in a fixed and uniform Cartesian grid. The VOSET method was utilised to capture the vapour–liquid interface (Sun & Tao 2010), while the IBM was applied to resolve the momentum exchange between particles and fluid (Kajishima, Takiguchi & Hamasaki 2001). Additionally, the DEM with soft-sphere collision model was used to calculate the collision forces $\boldsymbol{f_C}$ between solids (Tsuji, Kawaguchi & Tanaka 1993). This section provides a brief overview of the hybrid method, with details available in the literature (Chen, Yin & Dong 2024*a*,*b*).

The IDEAL algorithm was applied to solve the incompressible mass conservation equation and the Navier–Stokes equations to obtain the velocity field and pressure field (Sun *et al.* 2008*a*,*b*). The dimensionless governing equations are as follows:

$$\nabla \cdot \boldsymbol{u} = 0, \tag{3.1}$$

$$\frac{\partial \boldsymbol{u}}{\partial t} + (\boldsymbol{u} \cdot \nabla)\, \boldsymbol{u} = -\nabla p + \frac{1}{Re}\nabla^2 \boldsymbol{u} - \frac{1}{Fr}\boldsymbol{j} + \frac{1}{We}\boldsymbol{f_\sigma} + \boldsymbol{f_I}. \tag{3.2}$$

Herein, $\boldsymbol{u}$ is the velocity vector, t is time, p is pressure, $\boldsymbol{j} = \boldsymbol{g}/|\boldsymbol{g}|$ denotes the unit vector in the direction of the gravity and $\boldsymbol{g}$ is the gravitational acceleration. The Reynolds, Froude and Weber numbers are defined as $Re = \rho_l U L/\mu_l$, $Fr = U^2/gL$ and $We = \rho_l U^2 L/\sigma$, respectively, where U and L denote the characteristic velocity and length, μ_l is the liquid dynamic viscosity and σ is the surface tension coefficient.

The VOSET method is used to capture the vapour–liquid interface. The advection equation for the volume fraction C_f was solved to advance the vapour–liquid interface:

$$\frac{\partial C_f}{\partial t} + \nabla \cdot \left(\boldsymbol{u} C_f\right) = 0. \tag{3.3}$$

The geometric iterative algorithm was employed to solve the signed distance function ϕ in the vicinity of the interface. This method combines the excellent mass-conservation property of the volume-of-fluid method (Hirt & Nichols 1981) with the accurate evaluation of interface geometric properties provided by the level-set method (Sussman *et al.* 1996). Meanwhile, the computational cost is reduced by restricting the reconstruction ϕ to only a few grid layers around the interface, rather than updating ϕ throughout the entire computational domain.

The surface tension $\boldsymbol{f_\sigma}$ is calculated using our improved continuous surface force model (Popinet 2018; Chen, Yin & Dong 2024*b*):

$$\boldsymbol{f_\sigma} = -\sigma k \nabla H_\phi. \tag{3.4}$$

The curvature k of the vapour–liquid interface is solved using the height function technique (Popinet 2009). Function H_ϕ is the Heaviside function associated with the signed distance function ϕ.

The interaction force $\boldsymbol{f_I}$ between the particles and the fluid is calculated using the immersed solid method proposed by Kajishima *et al.* (2001). In this approach, a solid volume fraction field, C_s, is introduced to represent the local occupancy of the particle within each computational cell. The solid volume fraction is evaluated as (Yuki *et al.* 2007)

https://doi.org/10.1017/jfm.2026.11990 Published online by Cambridge University Press

$$C_s = \frac{1}{2}\left[1 - \tanh\left(\frac{\delta_p - R_p}{\lambda \xi \Delta x}\right)\right], \tag{3.5}$$

$$\lambda = |n_{p,x}| + |n_{p,y}|, \tag{3.6}$$

$$\xi = 0.3 + 0.05(1 - \lambda^2), \tag{3.7}$$

where δ_p is the distance between the grid node and the particle centre, R_p is the particle radius, Δx is the grid spacing, λ is an interface-orientation parameter, $\boldsymbol{n_p} = (n_{p,x}, n_{p,y})$ is the unit normal vector at the solid–liquid interface and ξ is an adaptive smoothing-width coefficient.

As the particle moves through the computational domain, the solid volume fraction field is recalculated at every time step using the instantaneous particle position and radius. Therefore, cells crossed by the moving particle are naturally treated through the continuous redistribution of C_s on the fixed Cartesian grid, without requiring mesh deformation or remeshing.

The local rigid-body velocity $\boldsymbol{u_s}$ of the particle is defined as

$$\boldsymbol{u_s} = \boldsymbol{v_s} + \boldsymbol{\omega_s} \times \boldsymbol{r_s}, \tag{3.8}$$

where $\boldsymbol{v_s}$ and $\boldsymbol{\omega_s}$ denote the translational and angular velocities of the particle, respectively, and $\boldsymbol{r_s}$ is the position vector measured from the particle centre.

The interaction force between the particle and the fluid is evaluated as

$$\boldsymbol{f_I} = \frac{C_s\left(\boldsymbol{u_s} - \boldsymbol{u_f^{F1}}\right)}{\Delta t}, \tag{3.9}$$

where $\boldsymbol{u_f^{F1}}$ is the intermediate fluid velocity obtained from solving the Navier–Stokes equations without considering the particle effect and Δt is the time step.

The corrected velocity field is then given by

$$\boldsymbol{u^{n+1}} = \boldsymbol{u_f^{F1}} + \Delta t\, \boldsymbol{f_I} = C_s \boldsymbol{u_s} + (1 - C_s)\boldsymbol{u_f^{F1}}. \tag{3.10}$$

Herein, $\boldsymbol{u^{n+1}}$ is the velocity after the immersed boundary correction. Consequently, the immersed boundary forcing constrains the velocity field within the particle region to follow the local rigid-body motion, while the interfacial cells provide a smooth transition between the fluid and solid phases. This treatment effectively enforces the no-slip condition on the moving particle surface.

Assuming the particle is a rigid sphere, its motion in the gas–liquid two-phase flow is governed by the gravitational force, the interaction force $\boldsymbol{F_p}$ from surrounding fluids and the collision forces $\boldsymbol{F_c}$ between the particle and the wall. Therefore, the translational and angular velocities of the solid particle can be obtained by applying Newton's law:

$$m_s \frac{\mathrm{d}\boldsymbol{v_s}}{\mathrm{d}t} = \boldsymbol{F_p} + \boldsymbol{F_c} + m_s \boldsymbol{g}, \tag{3.11}$$

$$\boldsymbol{I_s} \frac{\mathrm{d}\boldsymbol{\omega_s}}{\mathrm{d}t} = \boldsymbol{T_p} + \boldsymbol{T_c}, \tag{3.12}$$

where m_s is the mass of the particle, $\boldsymbol{I_s}$ is the inertia tensor, $\boldsymbol{T_p}$ is the interaction torque from surrounding fluids and $\boldsymbol{T_c}$ is the torque exerted by the collision force.

The particle–wall collision force $\boldsymbol{F_c}$ is computed using the DEM soft-sphere collision model. For particle–wall collisions, a consistent set of contact parameters is employed throughout the simulations. The coefficients of restitution in the normal and tangential

https://doi.org/10.1017/jfm.2026.11990 Published online by Cambridge University Press

directions are both set to 0.9. The normal and tangential spring stiffnesses are 800 and 80 N m^{-1}, respectively, and the friction coefficient is set to 0.3.

The interaction force $\boldsymbol{F_p}$ is determined by the integration of the fluid stress tensor over the particle surface:

$$\boldsymbol{F_p} = \int_S (-p\boldsymbol{I} + \boldsymbol{\tau}) \cdot \boldsymbol{n_p}\, \mathrm{d}S + \int_S (-\boldsymbol{\Pi}) \cdot \boldsymbol{n_p}\, \mathrm{d}S. \tag{3.13}$$

The first term on the right-hand side represents hydrodynamics, which includes pressure and viscous stress, and the second term represents capillary forces. Here, $\boldsymbol{\tau}$ denotes viscous stress and $\boldsymbol{\Pi}$ is the capillary pressure tensor. The tensor form of surface tension is introduced, expressed through the capillary pressure tensor (Lafaurie *et al.* 1994), which satisfies

$$\boldsymbol{f_\sigma} = -\nabla \cdot \boldsymbol{\Pi}. \tag{3.14}$$

According to the Gaussian divergence theorem, the integral of the hydrodynamic force terms over the particle surface can be equivalently expressed as the volume integral of these terms over the particle volume; similarly, the capillary force can also be obtained by performing a volume integration of the divergence of the capillary pressure tensor, which yields (Sun & Sakai 2016)

$$\boldsymbol{F}_p = \int_P \nabla \cdot (-p\boldsymbol{I} + \boldsymbol{\tau})\, \mathrm{d}V + \int_P \nabla \cdot (-\boldsymbol{\Pi})\, \mathrm{d}V. \tag{3.15}$$

Equation (3.2) in the fluid domain is integrated over the volume occupied by the particle:

$$\int_P \rho_f \frac{\mathrm{D}\boldsymbol{u}}{\mathrm{D}t}\, \mathrm{d}V = \int_P \left(-\nabla p + \nabla \cdot \boldsymbol{\tau} + \rho_f \boldsymbol{g} + \boldsymbol{f_\sigma} + \rho_f \boldsymbol{f_I}\right)\, \mathrm{d}V, \tag{3.16}$$

where ρ_f is the fluid density.

Substituting the expression for the total force exerted by the fluid on the particle into the above equation and rearranging the volume integral equation:

$$\boldsymbol{F_p} = \int_P \left(\frac{\mathrm{D}\boldsymbol{u}}{\mathrm{D}t} - \boldsymbol{g} - \boldsymbol{f_I}\right) \rho_f\, \mathrm{d}V. \tag{3.17}$$

Herein, the first term on the right-hand side is the inertial term caused by the acceleration of the particle motion. In the present study, the contribution of this inertial term is negligible compared with the hydrodynamic and capillary forces, and it is thus omitted. The second term represents the hydrostatic buoyancy force, which is separated from the dynamic interactions. The last term is the fluid–particle interaction force, which includes the hydrodynamic and capillary contributions.

Consequently, the governing equations for particle motion can be written as equations (3.18) and (3.19), where ΔV is the grid volume:

$$m_s \frac{\mathrm{d}\boldsymbol{v_s}}{\mathrm{d}t} = -\sum C_s \left(\boldsymbol{f_I} + \boldsymbol{g}\right) \rho_f \Delta V + \boldsymbol{F_c} + m_s \boldsymbol{g}, \tag{3.18}$$

$$\boldsymbol{I_s} \frac{\mathrm{d}\boldsymbol{\omega_s}}{\mathrm{d}t} = -\sum C_s \boldsymbol{r_s} \times \left(\boldsymbol{f_I} + \boldsymbol{g}\right) \rho_f \Delta V + \boldsymbol{T_c}. \tag{3.19}$$

The curvature at the boundary is corrected based on the height function to satisfy the contact angle boundary condition on the plane (Li & Lin 2023). The extension technique proposed by Sussman (2001) is adopted to satisfy the contact angle boundary condition on the particle surface, which is achieved by solving a specific convection equation:

https://doi.org/10.1017/jfm.2026.11990 Published online by Cambridge University Press

$$\frac{\partial C_f}{\partial \tau} + \boldsymbol{u}^{\boldsymbol{extend}} \cdot \nabla C_f = 0. \tag{3.20}$$

Herein, $\tau = 0.5\Delta x$ is the artificial time step. The variable $\boldsymbol{u}^{\boldsymbol{extend}}$ is the extension velocity for interface extrapolation, and the specific solution procedure can be found in the literature (Sussman 2001). In this study, the extension amount in the solid region is set to 4 grid sizes.

The numerical method has been systematically validated in our previous work through a series of benchmark problems, including particle sedimentation and particle impact onto a liquid pool (Chen, Yin & Dong 2024*b*). To further assess the accuracy and robustness of the present axisymmetric framework, additional validation cases are conducted, including particle sedimentation, bubble rising, bubble–particle interaction and particle impact onto a liquid pool. These benchmark cases cover a wide range of interfacial and fluid–particle interaction phenomena and demonstrate the capability of the proposed VOSET-IBM-DEM model to accurately capture particle motion, bubble dynamics, interface deformation and momentum exchange in axisymmetric three-phase flows. Detailed descriptions and quantitative comparisons with reference data are provided in the supplementary material available at https://doi.org/10.1017/jfm.2026.11990.

According to the grid resolution requirements of the validation cases, all simulations presented below are performed with a spatial resolution satisfying $D_p/\Delta x = 100$, and a fixed time step of $\Delta t = 2 \times 10^{-7}$ s is employed. The capillary time scale

$$t_c = \sqrt{\rho_l R_b^3/\sigma} \tag{3.21}$$

is adopted to characterise the bubble dynamics, where R_b is the bubble radius.

4. Results and discussion

4.1. *Bubble detachment modes*

The dynamic behaviour of a particle impacting a bubble under different Weber numbers ($We = \rho V^2 D_b/\sigma$) is investigated. Unless otherwise stated, the particle wettability was neutral ($\theta_p = 90°$), the density ratio was fixed at $k_\rho = 5.24$ and the size ratio at $k_r = 2/3$. The numerical results reveal three distinct detachment modes following impact: capillary-wave detachment (CWD), bubble-rebound detachment (BRD) and particle-rebound detachment (PRD). Representative snapshots of these modes are presented in figure 2.

At the early stage of the interaction, the dynamics bears strong resemblance to the coalescence of two droplets or bubbles (Eggers *et al.* 2024). Upon contact, a solid–vapour bridge rapidly forms at the point of impact. The bubble subsequently spreads over the particle surface, in a manner analogous to liquid-bridge growth, accompanied by the release of interfacial energy. A portion of this released surface energy is converted into capillary-wave energy, generating interfacial disturbances that propagate downstream along the vapour–liquid interface (Shi, Cui & Zhang 2015). Sustained excitation at the perturbed contact line leads to a transition from an initial single-pulse disturbance to a multi-period wave packet characterised by smaller leading waves followed by larger-amplitude trailing waves. This wave-packet structure is broadly consistent with the self-similar capillary-wave patterns reported by Ding *et al.* (2012). The detailed morphology is illustrated in figure 3. Point A denotes the primary crest adjacent to the particle contact line, whose evolution directly reflects local stress concentration. Points B and C correspond to the advancing crest and trough propagating towards the bottom surface, respectively. The wave packet exhibits pronounced spatio-temporal characteristics.

https://doi.org/10.1017/jfm.2026.11990 Published online by Cambridge University Press

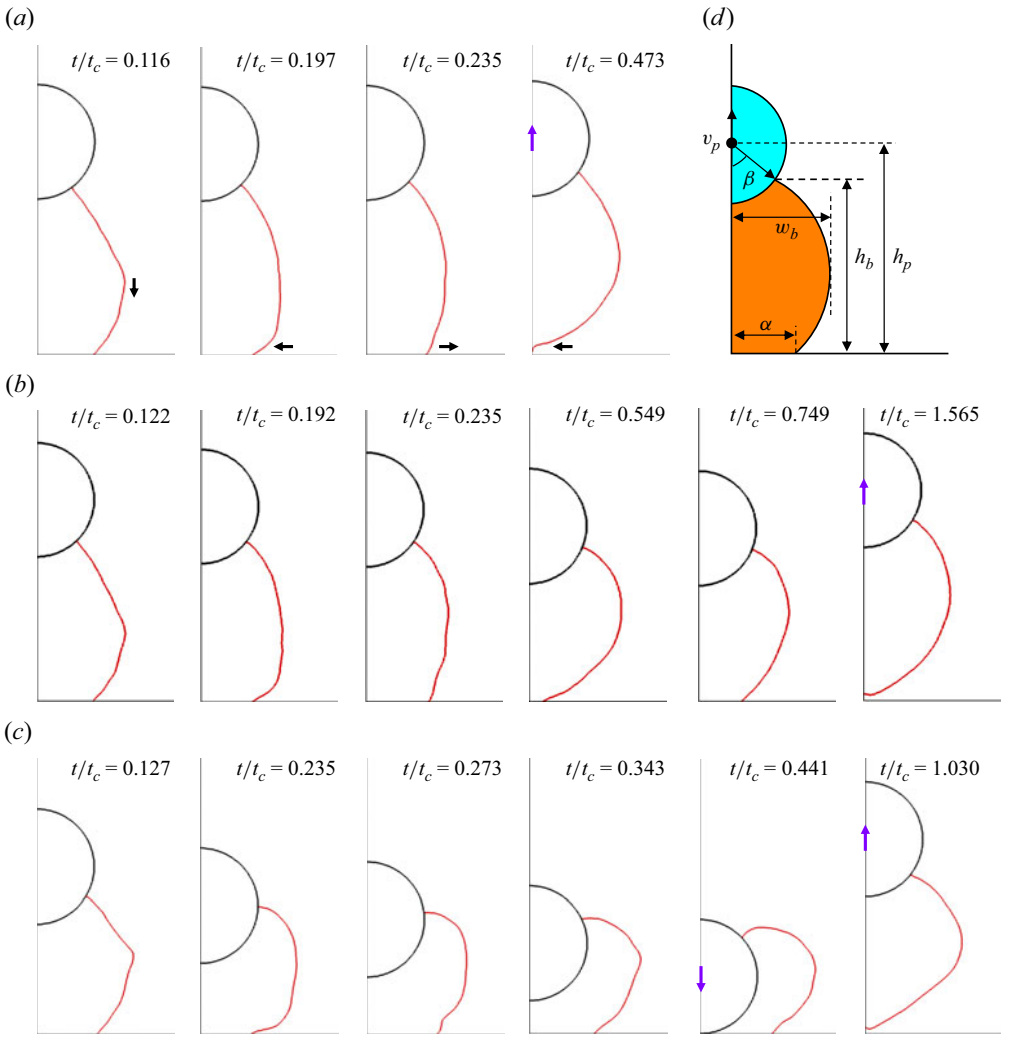


Figure 2. Bubble detachment modes induced by particle impact at different Weber numbers: (*a*) $We = 0.1$, CWD; (*b*) $We = 1.0$, BRD; (*c*) $We = 10$, PRD. (*d*) Schematic illustration of the key geometric parameters of the bubble.

In regions not yet reached by the capillary-wave front, the bubble remains quasi-static under the constraint of surface tension. In contrast, in regions traversed by the wave packet, the strong oscillations in interfacial curvature provide the energetic basis for subsequent momentum redistribution. The first column of figure 2 shows the transient configuration prior to disturbance of the bottom contact line. The results indicate that, with increasing *We*, the time required for the capillary wave to reach the bubble base increases slightly.

When the capillary wave packet reaches the bottom surface, the three-phase contact line at the substrate is set into motion under wave-induced forcing. Figure 4 presents the temporal evolution of the dimensionless contact radius, $k_\alpha = \alpha/\alpha_0$. The initial geometric parameters of the bubble–particle system are defined in figure 1, and the characteristic length scales during impact are illustrated in figure 2(*d*). The contact line first undergoes a retraction driven by the leading small-amplitude wave (second column of figure 2), followed by an initial spreading phase (third column), with the maximum spreading radius

https://doi.org/10.1017/jfm.2026.11990 Published online by Cambridge University Press

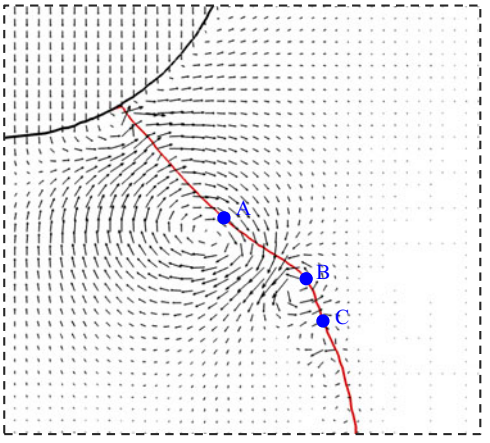


Figure 3. Structure of capillary waves.

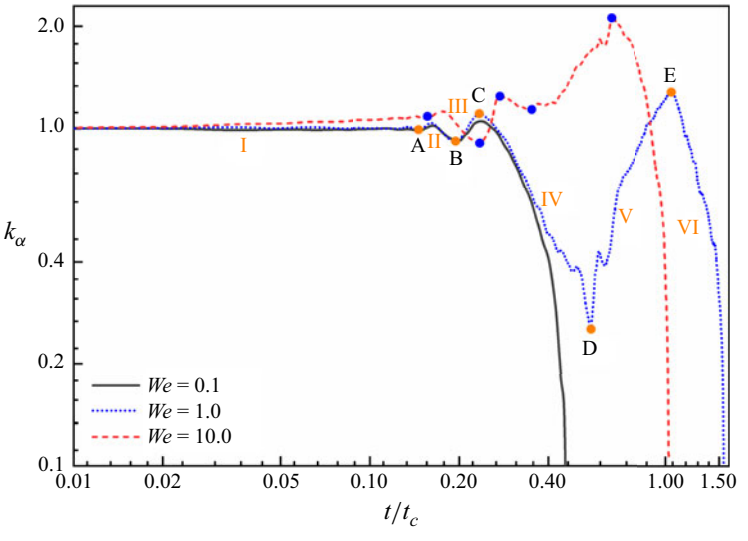


Figure 4. Temporal evolution of the dimensionless bottom contact radius.

increasing monotonically with *We*. Subsequently, a second retraction occurs under the action of the larger trailing wave (fourth column). At $We = 0.1$, the bubble detaches directly from the substrate at $t/t_c = 0.473$. In this regime, detachment is governed primarily by the large trailing wave. This wave-driven mechanism is termed CWD. Based on the contact-line dynamics at the bottom surface, the process can be divided into four stages: a quasi-static stage (I), a first retraction stage (II), a first spreading stage (III) and a second retraction stage (IV). Stages II–IV are all driven by capillary-wave forcing.

For $We = 1.0$ and 10, detachment does not occur directly during stage IV. The extent of the second retraction decreases markedly with increasing *We*, indicating that particle inertia suppresses the capillary-driven contact-line motion, with the degree of suppression positively correlated with impact velocity. For $We = 1.0$, the particle velocity decreases to zero at $t/t_c = 0.749$. Owing to prior compression, the bubble has accumulated potential energy, which is subsequently released to induce a rebound motion, carrying the particle

https://doi.org/10.1017/jfm.2026.11990 Published online by Cambridge University Press

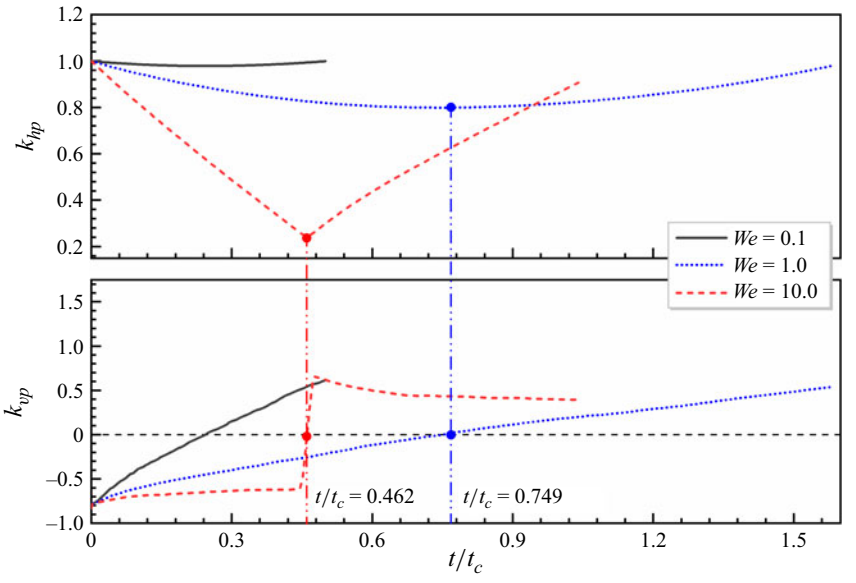


Figure 5. Temporal evolution of the dimensionless particle position and velocity.

upward synchronously. The bubble eventually detaches at $t/t_c = 1.565$. This mode, driven by the recovery of bubble deformation, is defined as BRD. Compared with CWD, BRD involves two additional stages: a secondary spreading stage (V), resulting from particle-induced suppression, and a third retraction stage (VI), triggered by bubble rebound.

At $We = 10$, the substantially larger initial kinetic energy of the particle causes it to strike the substrate directly at $t/t_c = 0.441$, followed by mechanical rebound. During this collision, the bubble undergoes more severe compression. Thereafter, the release of bubble potential energy acts synergistically with particle rebound, jointly driving the coupled particle–bubble system upward and leading to detachment at $t/t_c = 1.030$. This mode is defined as PRD. Its evolution also comprises six stages. The first five stages are essentially identical to those of BRD, whereas stage VI corresponds to a third retraction induced by the combined rebound of both the bubble and the particle.

A comparison of detachment times among the three modes shows that CWD, involving the fewest dynamical stages, yields the shortest detachment time (0.473), followed by PRD (1.030), while BRD exhibits the longest detachment time (1.565). The difference between BRD and PRD arises from their distinct rebound-response mechanisms (Chen *et al.* 2019). Figure 5 shows the temporal evolution of the dimensionless particle position, $k_{h_p} = h_p/H_p$, and velocity, $k_{v_p} = v_p/V$. The bubble responds analogously to a soft spring: its compression and rebound are gradual, and the feedback to particle motion is delayed. By contrast, particle impact with the substrate is a typical elastic collision characterised by an impulsive response and extremely high acceleration. Consequently, although the contact area at rebound under $We = 10$ is larger than that at $We = 1.0$, the much higher initial rebound velocity shortens the time interval between rebound onset and complete detachment.

4.2. *Surface energy conversion and geometric suppression*

From the perspective of the coupled bubble–particle dynamics, the first four stages of detachment are primarily governed by capillary-wave forcing at the bottom contact line. The underlying energy source can be traced to the surface energy released during bubble

https://doi.org/10.1017/jfm.2026.11990 Published online by Cambridge University Press

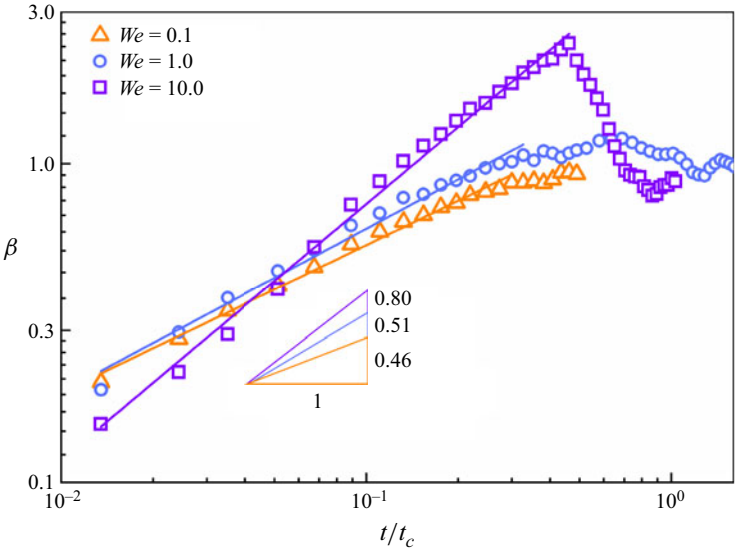


Figure 6. Temporal evolution of the spreading angle of the bubble on the particle surface.

spreading over the particle surface. In studies of droplet coalescence dynamics (Eggers *et al.* 2024), the evolution of the liquid-bridge radius r_l is commonly employed as a key metric for quantifying the rate of energy conversion. By analogy, in the present configuration the local vapour–liquid interfacial variation is predominantly induced by bubble wetting and spreading over the particle.

To quantify this process, we introduce the spreading angle β to characterise the extent of surface energy release. When the spreading angle reaches β, the corresponding reduction in the local vapour–liquid interfacial area, ΔS, is equivalent to the area of a spherical cap with central angle β:

$$\Delta S = 2\pi R_p^2(1-\cos\beta). \tag{4.1}$$

The instantaneous release rate of surface energy is given by

$$\dot{E}_s = \gamma \frac{\mathrm{d}(\Delta S)}{\mathrm{d}t}, \tag{4.2}$$

where γ is the vapour–liquid surface tension.

Figure 6 shows the evolution of the spreading angle β as a function of the dimensionless time t/t_c for different *We*. During the early spreading stage, β follows a power-law scaling:

$$\beta \sim \left(\frac{t}{t_c}\right)^b. \tag{4.3}$$

For $We = 0.1$, 1 and 10, the exponent b is 0.46, 0.51 and 0.80, respectively. The increase in b reflects the enhanced wetting dynamics induced by particle impact. For $We \leq 1$, the system resides in a capillary-dominated spreading regime, with $b \approx 0.5$, consistent with the inertial-capillary limit (De Maleprade *et al.* 2016). When $We > 1$, mechanical kinetic energy directly participates in interfacial evolution, accelerating the surface energy release rate. As a result, higher *We* leads to a greater amount of surface energy released per unit time, thereby exciting capillary waves of higher energy density.

In addition to surface energy release, particle impact induces global bubble deformation, thereby modifying its potential energy distribution. To assess this effect, the horizontal

https://doi.org/10.1017/jfm.2026.11990 Published online by Cambridge University Press

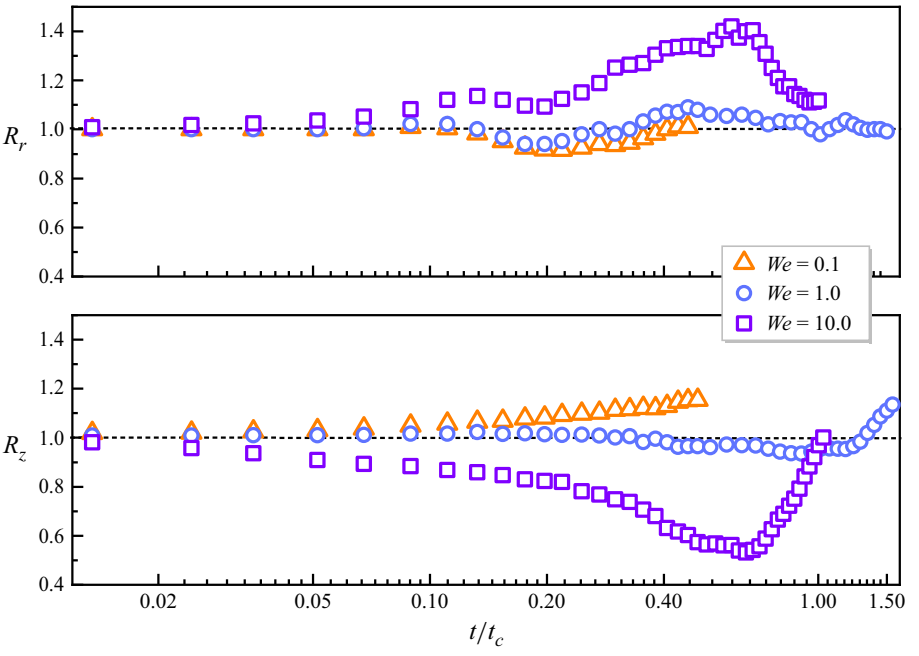


Figure 7. Temporal evolution of the bubble dimensions in the horizontal and vertical directions.

($R_r = w_b/W_b$) and vertical ($R_z = h_b/H_b$) characteristic dimensions of the bubble are introduced, and their temporal evolutions are shown in figure 7. For $We = 0.1$, spreading-induced axial elongation dominates, leading to an increase in the vertical extent. This elongation provides a geometrical 'pre-tension' that facilitates subsequent contact-line retraction and promotes capillary-wave-driven detachment. By contrast, at $We = 10$, strong particle impact leads to dominant compressive deformation. The vertical dimension decreases progressively after impact, which limits the energy density available when capillary waves converge towards the axis. Consequently, despite greater total surface energy release, the conversion into effective upward momentum is hindered. Bubble detachment therefore results from a dynamic competition between surface energy release and mechanically induced compressive suppression. Although large We enhances the energetic source term (surface energy release), the severe geometric deformation and negative momentum injection associated with impact offset the capillary-wave driving effect, rendering capillary-wave-induced detachment less likely.

4.3. *Momentum evolution during particle impact*

To quantify the momentum accumulation of the bubble during particle impact, the analysis is conducted within the framework of Kelvin impulse theory. According to potential-flow theory, the Kelvin impulse $\boldsymbol{I}$ is defined as the surface integral of the velocity potential φ over the bubble surface S_b (Best & Blake 1994; Wang *et al.* 2022):

$$\boldsymbol{I} = \oint_{S_b} \rho_l \varphi \boldsymbol{n} \, \mathrm{d}S, \tag{4.4}$$

where $\boldsymbol{n}$ is the unit normal vector directed into the bubble.

By virtue of the divergence theorem, the surface integral over a closed surface can be converted into a volume integral of its divergence. To extract the vertical component I_z,

https://doi.org/10.1017/jfm.2026.11990 Published online by Cambridge University Press

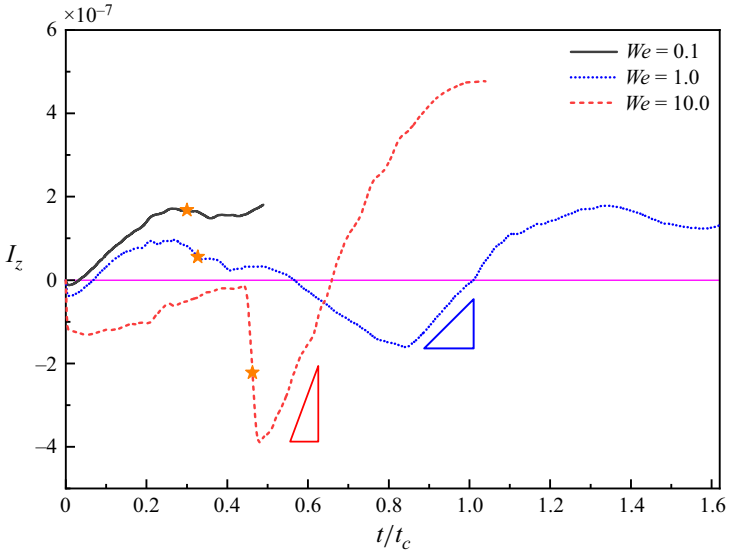


Figure 8. Temporal evolution of the vertical Kelvin impulse.

we construct the auxiliary vector field $\boldsymbol{A} = \varphi \boldsymbol{k}$, where $\boldsymbol{k}$ is the unit vector in the vertical direction. Application of the divergence theorem yields

$$\oint_{S_b} \phi \boldsymbol{n} \cdot \boldsymbol{k} \, \mathrm{d}S = \int_{V_b} \nabla \cdot (\phi \boldsymbol{k}) \, \mathrm{d}V. \tag{4.5}$$

The velocity field is defined as $\boldsymbol{u} = \nabla \varphi$, and hence $\nabla \cdot (\varphi \boldsymbol{k}) = u_z$, the vertical velocity component. Substitution leads to the volume-integral representation of the Kelvin impulse:

$$I_z = \rho_l \int_{V_b} u_z \, \mathrm{d}V, \tag{4.6}$$

which can be interpreted as an equivalent vertical momentum associated with the liquid motion within the bubble volume. Its discrete form reads

$$I_z = \rho_l \sum_{i=1}^{N} (u_z)_i F_i \Delta V_i, \tag{4.7}$$

where F_i denotes the vapour volume fraction and ΔV_i the cell volume.

Figure 8 shows the temporal evolution of I_z for different We. At the initial stage of impact, increasing We enhances the downward momentum injected by the particle, resulting in a pronounced negative peak of I_z. Subsequently, under the action of capillary waves excited by surface energy release, the negative impulse gradually decays in all cases. For $We \leq 1$, the initial downward impulse is relatively small, and the capillary-wave-induced positive momentum accumulation rapidly overcomes inertial suppression, leading to momentum reversal ($I_z > 0$). The star symbol in the figure marks the transition point of the spreading power law, beyond which contact-line spreading approaches saturation and the spreading rate decreases.

At $We = 0.1$, although the spreading transition point is crossed, the impulse evolves smoothly owing to the weak impact. Capillary waves are therefore sufficient to directly induce bubble detachment. At $We = 1$, capillary waves initially promote partial recovery of the impulse; however, substantial energy is consumed in overcoming substrate adhesion, and continued particle compression imposes geometric suppression. As a result, the total

https://doi.org/10.1017/jfm.2026.11990 Published online by Cambridge University Press

impulse turns negative again after approaching zero. Only when the particle velocity decreases to zero does the stored deformation energy of the bubble dominate the rebound, ultimately triggering detachment. In contrast, at $We = 10$, the particle remains in the spreading power-law regime prior to substrate impact, and the large impact momentum maintains a persistently negative vertical impulse. Upon collision, mechanical rebound of the particle induces an abrupt and strong momentum reversal, causing I_z to increase sharply with a steep slope and thereby driving rapid detachment.

The temporal rate of change of the Kelvin impulse represents the resultant force acting on the bubble (Best & Blake 1994):

$$F = \frac{\mathrm{d}I_z}{\mathrm{d}t}. \tag{4.8}$$

As shown in the figure, compared with the BRD case ($We = 1.0$), the impulse curve in the PRD regime ($We = 10$) exhibits a markedly steeper slope. This indicates that under the collision-induced rebound mechanism, the system acquires a stronger instantaneous positive upward impulse, thereby substantially enhancing the efficiency of bubble detachment.

To quantify the effectiveness of energy utilisation under different detachment modes, an energy efficiency ratio η_e is introduced:

$$\eta_e = \frac{E_{k,b}}{E_{available}} = \frac{E_{k,b}}{\Delta E_s + W_{p,rebound}}, \tag{4.9}$$

where $E_{k,b}$ denotes the effective detachment kinetic energy defined via the Kelvin impulse:

$$E_{k,b} = \frac{I_{z,detach}^2}{2M_{added}} = \frac{I_{z,detach}^2}{2\rho_l V_b}. \tag{4.10}$$

Herein, $I_{z,detach}$ denotes the vertical component of the Kelvin impulse at the instant of bubble detachment and M_{added} is added mass. To maintain consistency with the volume-integral form of the Kelvin impulse, the added mass is defined as the mass of liquid displaced by the bubble ($M_{added} = \rho_l V_b$). This definition is consistent with potential-flow inertia for bodies moving near boundaries and appropriately quantifies the directed detachment energy transferred to the surrounding liquid.

The available input energy $E_{available}$ consists of the surface energy ΔE_s released during spreading and, in the particle-rebound mode, the mechanical rebound energy $W_{p,rebound}$ of the particle. The capillary-wave energy driving contact-line motion primarily originates from the released surface energy during the first stage:

$$\Delta E_s = \sigma\left[(A_{lv} - A_{sl}\cos\theta_p)_{b,initial} - \left(A_{lv} - A_{sl}\cos\theta_p\right)_{b,min}\right], \tag{4.11}$$

where A_{lv} and A_{sl} denote the vapour–liquid and vapour–solid interfacial areas, respectively. In the present cases, $\theta_p = 90°$, so that the surface energy variation reduces to (Nam, Kim & Shin 2013)

$$\Delta E_s = \sigma[(A_{lv})_{b,initial} - (A_{lv})_{b,min}]. \tag{4.12}$$

The particle rebound energy, included only in the PRD mode, characterises the directional mechanical energy injected into the flow through collision:

$$W_{p,rebound} = \frac{1}{2} m_p v_{r,max}^2, \tag{4.13}$$

where $v_{r,max}$ is the maximum rebound velocity.

https://doi.org/10.1017/jfm.2026.11990 Published online by Cambridge University Press

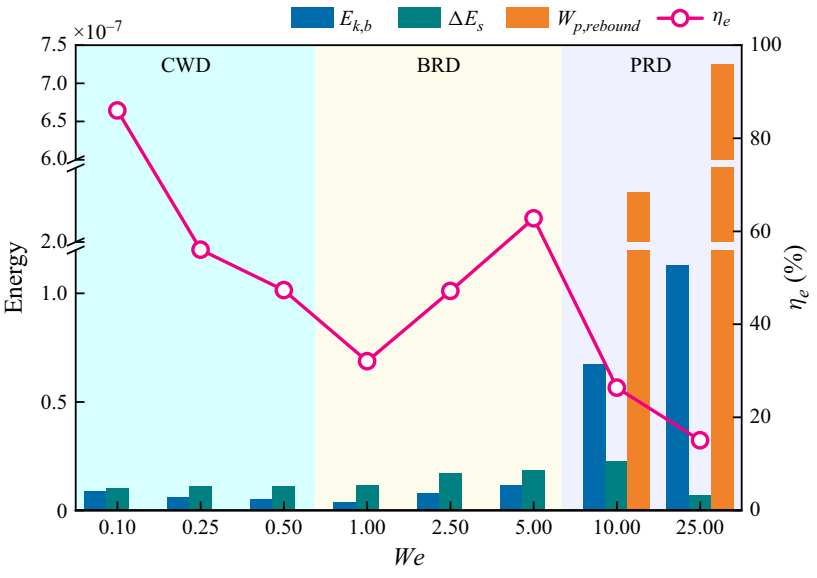


Figure 9. Energy and energy utilisation efficiency at different Weber numbers.

Figure 9 presents the energy components and energy efficiency ratio η_e for different We. For $We \leq 10$, the released surface energy generally increases with We, consistent with the power-law spreading behaviour discussed previously. This observation further confirms that the surface energy variation in stage I mainly originates from bubble spreading over the particle surface. At $We = 25$, despite the substantial spreading induced by particle impact, the bubble undergoes pronounced compression. As a result, the net variation of the total interfacial area remains small, leading to a reduced release of surface energy. The kinetic energy at detachment strongly depends on the detachment regime. In the CWD regime, increasing We promotes surface energy release, whereas the detachment kinetic energy decreases, indicating a reduced efficiency of energy conversion. This behaviour can be attributed to the enhanced compression of the bubble, which consumes an increasing fraction of the released surface energy.

After the transition to the BRD regime, both the detachment kinetic energy and η_e increase with We. Stronger impacts lead to more significant bubble compression, enabling more potential energy to be stored in the deformed interface and released during the rebound process. Consequently, the upward impulse generated at detachment becomes stronger, leading to a higher energy efficiency ratio η_e.

Following the transition to the PRD regime, the rebound of the particle injects substantial directional momentum into the flow, causing the detachment kinetic energy to increase with We. In this regime, the rebound energy of the particle becomes the dominant energy contribution, reaching 10.3 and 102.2 times the released surface energy for $We = 10$ and 25, respectively. Despite the substantial mechanical energy supplied by particle rebound, η_e remains relatively low. A large fraction of the rebound energy is dissipated through viscous effects and particle deceleration during the subsequent upward motion, while only a limited portion contributes to bubble detachment. The further reduction of efficiency from $We = 10$ to 25 indicates that energy dissipation becomes increasingly important at higher We.

Particle wettability, geometric size and density play decisive roles in governing the post-impact spreading, wetting behaviour and deformation evolution of the bubble.

https://doi.org/10.1017/jfm.2026.11990 Published online by Cambridge University Press

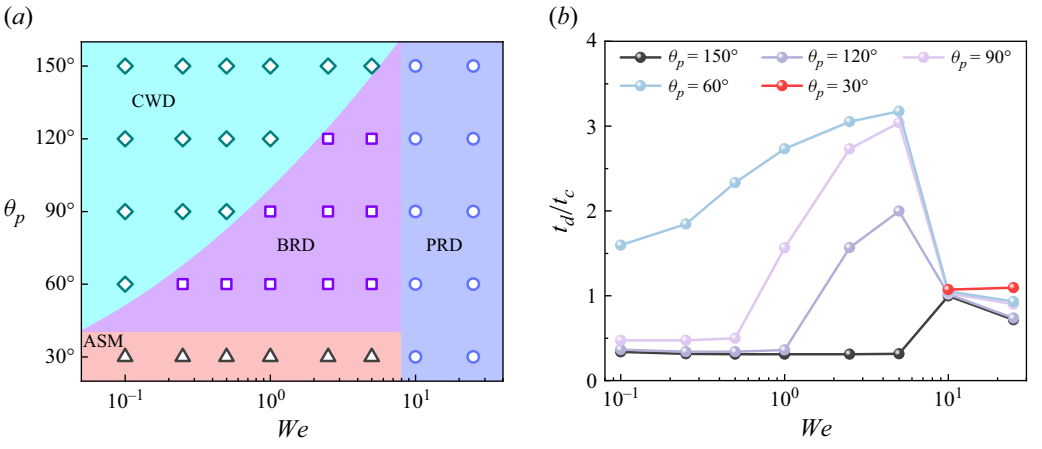


Figure 10. (*a*) Detachment regime map and (*b*) detachment time of the bubble at different Weber numbers and particle wettabilities.

In the following sections, these factors are systematically investigated to elucidate their respective influences on the impact dynamics.

4.4. *Synergistic effects of impact We and particle wettability*

The synergistic influence of the impact Weber number and particle wettability on system dynamics was studied, as discussed in this section. The parameter ranges considered are $0.1 \leq We \leq 25$ and $30° \leq \theta_p \leq 150°$, with density ratio $k_\rho = 5.24$ and size ratio $k_r = 2/3$. The resulting detachment-mode map is presented in figure 10(*a*). For $\theta_p \geq 90°$ and $We \leq 1$, CWD dominates, and its regime expands towards higher We as θ_p increases. In contrast, for hydrophilic particles ($\theta_p = 30°$), the system remains in the adhered-sedimentation mode (ASM) for $We < 10$. At intermediate contact angles and moderate We, BRD prevails. Once We exceeds a critical threshold (approximately 10), the system transitions to PRD. Notably, the onset boundary of PRD exhibits weak sensitivity to wettability, indicating that under strong inertial impact, externally injected mechanical work largely overrides interfacial differences induced by θ_p.

The corresponding evolution of the dimensionless detachment time, t_d/t_c, is shown in figure 10(*b*). Under CWD dominance, t_d/t_c remains at a relatively low and nearly constant level, displaying little sensitivity to We. However, as θ_p decreases from hydrophobic to hydrophilic, t_d/t_c increases progressively and becomes increasingly sensitive to wettability. This reflects the highly transient nature of capillary-wave-driven detachment, which is not constrained by prolonged inertial suppression cycles. In the BRD regime, t_d/t_c increases significantly and exhibits a trend of increasing with We and decreasing with θ_p. This behaviour correlates closely with the time required for the particle velocity to decay to zero. As We increases, deeper particle penetration extends the energy storage period, while limited contact-line mobility under less hydrophobic conditions prolongs morphological recovery before detachment can occur. In the PRD regime, enhanced mechanical energy compensation reduces the disparity in t_d/t_c across wettabilities. Owing to the impulsive nature of particle–substrate collision, the high-amplitude rebound force generated over a short duration disrupts the quasi-static balance of bubble deformation recovery, leading to overall shorter detachment times than in BRD.

As established previously, the essence of CWD lies in whether the initial capillary-wave packet can overcome substrate adhesion and geometric suppression induced by particle

https://doi.org/10.1017/jfm.2026.11990 Published online by Cambridge University Press

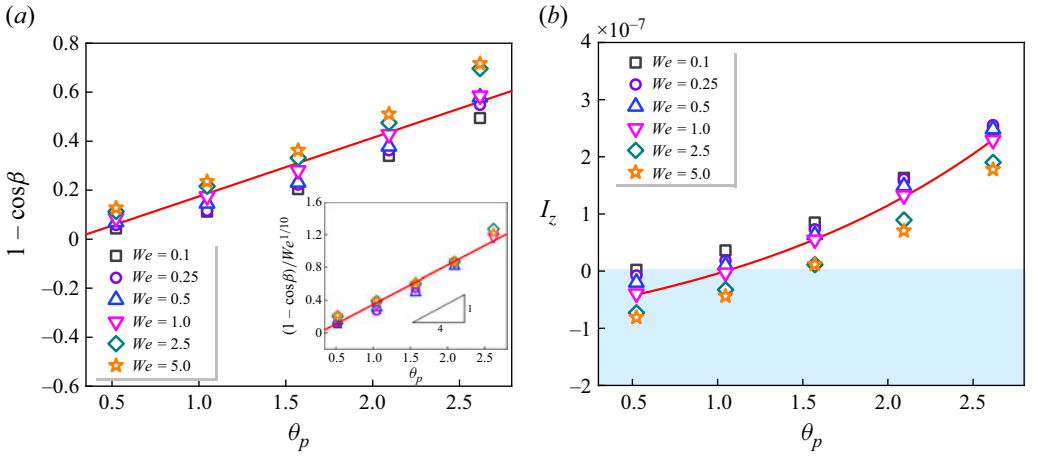


Figure 11. (*a*) Bubble spreading angle and (*b*) vertical impulse at $t/t_c = 0.127$ under different Weber numbers and particle wettabilities.

compression. The energy of this wave packet originates primarily from surface energy released during bubble spreading over the particle (Chen *et al.* 2025*a*). According to (4.1) and (4.2), the associated energy-conversion rate scales positively with $R_p^2(1-\cos\beta)$. Since R_p is fixed in the present study, the value of $(1-\cos\beta)$ at the end of stage I ($t/t_c = 0.127$) is used to quantify spreading-induced surface energy variation. Figure 11(*a*) shows the dependence of $(1-\cos\beta)$ on θ_p and *We*. The results indicate positive correlations with both parameters. Scaling analysis reveals that the normalised spreading factor obeys the power law

$$(1-\cos\beta) \propto \theta_p We^{1/10}. \tag{4.14}$$

Thus, the normalised $(1-\cos\beta)$ increases linearly with θ_p (slope 1/4) and follows a weak power-law dependence on *We* (exponent 1/10), indicating stronger sensitivity to wettability than to inertia.

To further quantify capillary-wave-driven detachment capability, the vertical impulse I_z at $t/t_c = 0.127$ is extracted from figure 11(*b*). The impulse increases markedly with θ_p but decreases with increasing *We*. For $We \leq 1$, I_z is primarily governed by contact angle and only weakly affected by inertia. For $We \geq 1$, however, the impulse reflects a coupled regulation by both *We* and wettability. At fixed θ_p, I_z is more sensitive to *We* than the spreading factor $(1-\cos\beta)$. In particular, when $We \geq 1$, the reduction in I_z with increasing *We* becomes substantial, demonstrating that inertial suppression outweighs spreading enhancement. Under high-*We*, low-θ_p conditions, I_z becomes negative, indicating that strong inertial compression fully offsets capillary-wave-driven upward motion.

These observations highlight a competition between 'spreading gain' (favouring detachment) and 'inertial suppression' (hindering detachment) as *We* increases at fixed θ_p. To quantify this balance, a bubble detachment capability factor η is introduced, defined at $t/t_c = 0.127$ as

$$\eta = \mathrm{sgn}\,(I_z)\,\frac{E_{k,b}}{\Delta E_s}, \tag{4.15}$$

https://doi.org/10.1017/jfm.2026.11990 Published online by Cambridge University Press

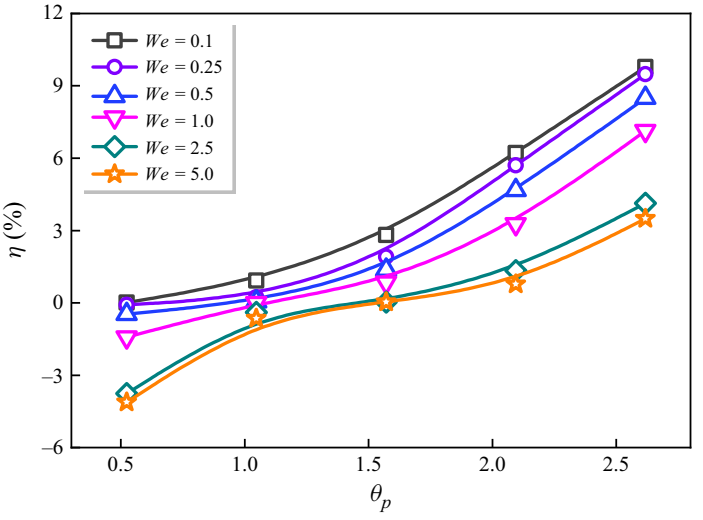


Figure 12. Bubble detachment capability factor η under different We and θ_p.

where sgn(I_z) accounts for impulse direction (+1 for $I_z \geq 0$, −1 otherwise), $E_{k,b}$ is the upward kinetic energy of the bubble and ΔE_s is the released surface energy.

Figure 12 illustrates the variation of η under the combined effects of θ_p and We. The efficiency increases monotonically with θ_p, reaching particularly high values in the hydrophobic regime at low We. This confirms, from an energetic perspective, that enhanced hydrophobicity promotes conversion of interfacial potential energy into vertical kinetic energy, thereby facilitating detachment. Conversely, η decreases with increasing We across all wettabilities, and the decline becomes more pronounced at higher We. Under extreme high-We, low-θ_p conditions, η crosses zero and becomes negative, corresponding to the negative impulse distribution in figure 11(*b*). In this regime, strong impact inertia not only dissipates released surface energy but also drives downward motion, leading to the ASM state. Taken together with the interfacial evolution and momentum distribution shown in figure 11, it is evident that although increasing We enhances surface energy release via stronger spreading (higher $(1 - \cos\beta)$), the accompanying downward inertial suppression dominates in magnitude, thereby limiting the potential for capillary-wave-driven detachment.

In the PRD regime, the primary driving mechanisms for detachment are the mechanical rebound kinetic energy generated upon particle–substrate collision and the elastic potential energy stored in bubble deformation. To quantify the influence of particle wettability on PRD behaviour, the dimensionless maximum rebound velocity, $k_{vp_r} = v_{p_r}/V_0$, and the bubble shape factor at rebound, $k_{br} = R_{br}/R_{bz}$, are examined. The results are presented in figure 13, which also includes representative snapshots at $We = 10$ corresponding to the instant of maximum particle rebound velocity for different contact angles. The maximum rebound velocity increases monotonically with θ_p. A larger contact angle reduces the spreading resistance of the bubble over the particle surface, thereby facilitating particle penetration through the bubble and diminishing momentum dissipation during descent. When $\theta_p = 120°$, the particle has already fully penetrated the bubble before attaining its maximum rebound velocity.

In contrast, the bubble size ratio k_{br} decreases with increasing θ_p. A smaller k_{br} corresponds to stronger bubble compression and hence greater storage of elastic potential energy available for rebound (Liu *et al.* 2014). These two opposing trends – enhanced

https://doi.org/10.1017/jfm.2026.11990 Published online by Cambridge University Press

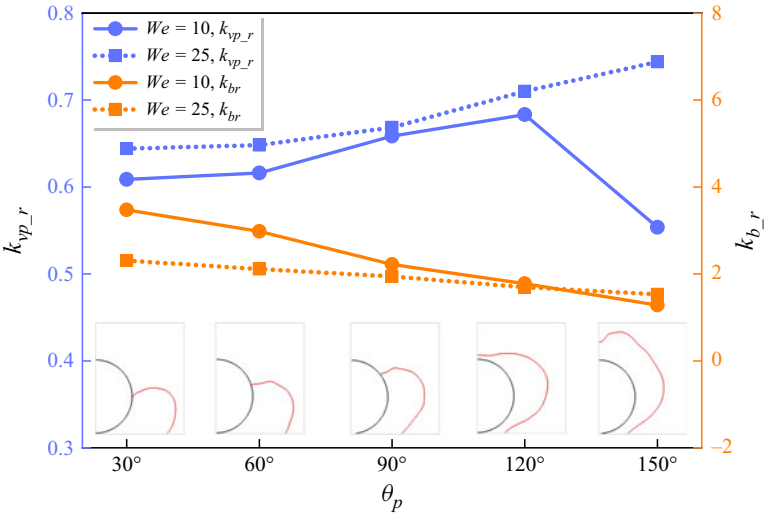


Figure 13. Maximum rebound velocity of the particle and bubble shape factor at different θ_p.

particle rebound velocity but reduced bubble compression at higher θ_p – compensate each other, leading to relatively small variations in detachment time within the PRD regime at high *We*. It is noteworthy that at $\theta_p = 150°$ and $We = 10$, a slight local reduction in rebound performance is observed. However, when *We* increases to 25, the intensified mechanical energy input effectively overcomes this limitation, ensuring efficient bubble detachment under strong-impact conditions.

4.5. *Synergistic effects of impact We and density ratio*

The coupled influence of the impact Weber number ($0.1 \leq We \leq 10$) and the particle–liquid density ratio ($1 \leq k_\rho \leq 10$) was systematically investigated, as discussed in this section. The particle contact angle is fixed at 90°, and the particle-to-bubble size ratio is $k_r = 2/3$. The detachment-mode phase diagram is presented in figure 14(*a*). An increase in density ratio essentially enhances the mass inertia of the system. At a fixed *We*, particles with higher k_ρ possess greater downward momentum, intensifying interfacial compression and energy dissipation. Consequently, the density ratio markedly shifts the threshold boundaries between detachment modes. As k_ρ increases from 1.0 to 10.0, the control region of CWD contracts towards lower *We*, while the ASM gradually emerges at high density ratios. At $We = 10$, PRD remains dominant. Owing to the stronger inertial effect associated with large k_ρ ($= 10$), the transition to PRD is triggered earlier, occurring already at $We = 2.5$.

Figure 14(*b*) shows the variation of the dimensionless detachment time t_d/t_c. In the CWD regime, the detachment time is nearly insensitive to density ratio, indicating that under weak-impact conditions, system dynamics remains governed by capillary-wave energy, and particle mass differences do not yet introduce significant geometric suppression. For high-density particles, t_d/t_c exhibits a pronounced nonlinear jump, corresponding to the BRD regime. Deeper penetration by heavier particles prolongs the period of energy storage and morphological recovery, forming a clear dynamical bottleneck. Once the system enters the PRD regime, t_d/t_c rapidly decreases and converges across different density ratios. This suggests that for high-mass systems, the strong mechanical work supplied by particle rebound becomes the decisive factor in overcoming interfacial adhesion and shortening the detachment cycle.

https://doi.org/10.1017/jfm.2026.11990 Published online by Cambridge University Press

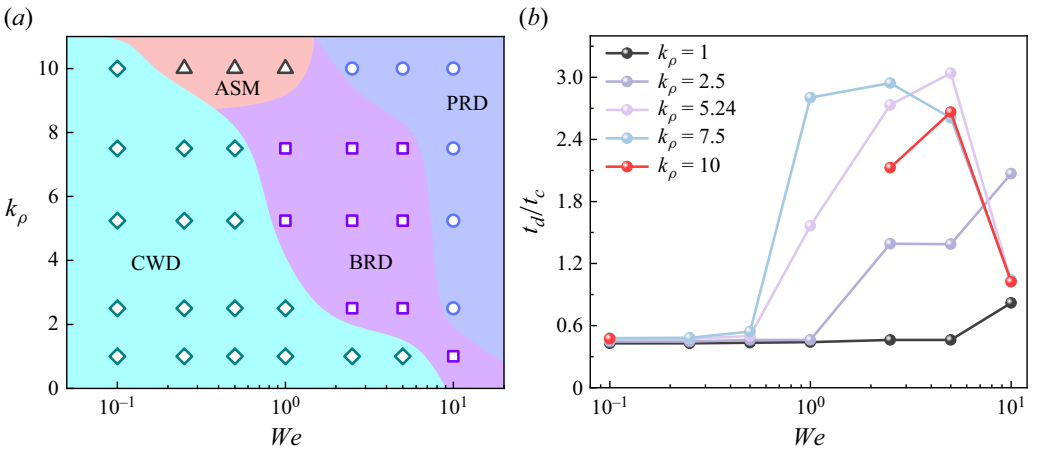


Figure 14. (*a*) Detachment regime map and (*b*) detachment time of the bubble at different Weber numbers and density ratios.

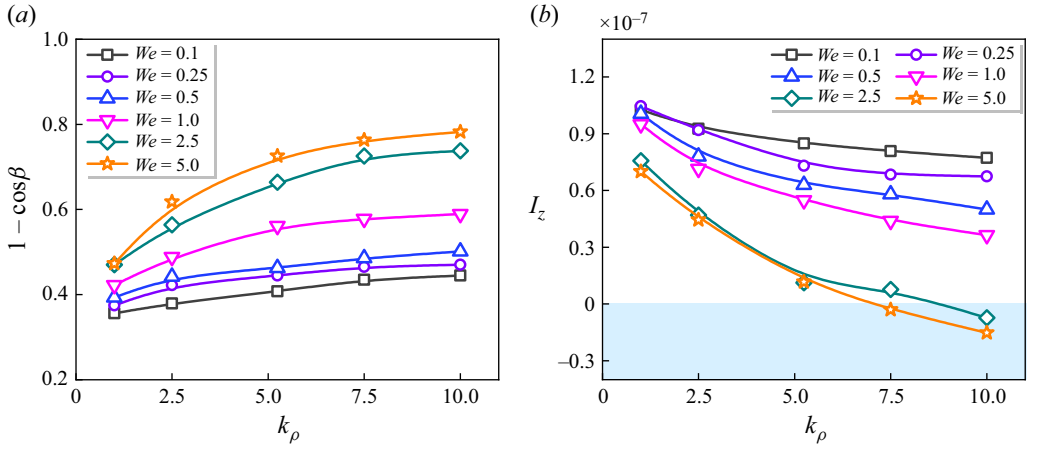


Figure 15. (*a*) Bubble spreading angle and (*b*) vertical impulse at $t/t_c = 0.127$ at various *We* and k_ρ.

Figure 15(*a*) presents the variation of local surface energy change at the end of the initial spreading stage ($t/t_c = 0.127$), characterised by $(1 - \cos\beta)$, as functions of k_ρ and *We*. Over the entire *We* range, the interfacial energy variation increases monotonically with k_ρ, although the growth rate gradually diminishes and becomes nearly saturated for $k_\rho > 7.5$. Additionally, $(1 - \cos\beta)$ increases significantly with *We*. Mechanistically, high-density particles not only carry greater initial kinetic energy but also exhibit stronger resistance to deceleration, maintaining high-speed penetration for a longer duration during bubble compression. This sustained impact forces more pronounced radial expansion of the contact line, promoting surface energy release. In contrast, the vertical impulse I_z displays a distinctly negative evolution trend, as shown in figure 15(*b*). With increasing k_ρ or *We*, I_z decreases monotonically. The decline rate becomes less sensitive to density ratio at high k_ρ but intensifies with increasing *We*. Under combined high-k_ρ and high-*We* conditions, I_z rapidly crosses zero and enters a deeply negative regime. This indicates that inertia-induced downward compression dominates the vertical momentum balance, and the released capillary-wave driving force is insufficient to counteract the downward

https://doi.org/10.1017/jfm.2026.11990 Published online by Cambridge University Press

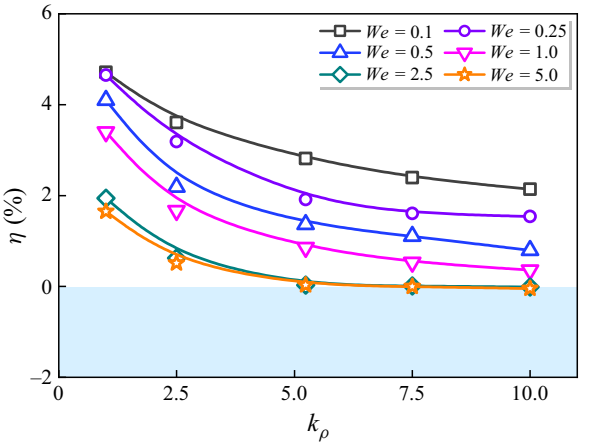


Figure 16. Bubble detachment capability factor η under different We and k_ρ.

traction imposed by heavy particles, thereby promoting transitions between detachment modes.

Figure 16 illustrates the evolution of the bubble detachment efficiency factor η. The efficiency decays approximately exponentially with increasing k_ρ, with the most pronounced attenuation occurring at intermediate We. This suggests that in this range, gravitational (mass-related) and impact inertial effects are comparable in magnitude, rendering the system highly sensitive to density variation. At low We (< 0.25), capillary-wave dynamics dominates momentum response, and η remains relatively high across all density ratios. At higher We ($\geq$2.5), impact inertia prevails. Although the synergistic increase of density and inertia enhances surface energy release, the fraction converted into upward kinetic energy decreases sharply and may even become negative. Particularly when $We \geq 2.5$ and $k_\rho > 5.0$, η approaches zero or becomes negative. In this regime, despite severe interfacial deformation, energy cannot be effectively released in the vertical direction, and the system transitions from CWD to other modes.

For the PRD regime at high impact inertia ($We = 10.0$), figure 17 presents the maximum particle rebound velocity k_{vp_r} and the bubble shape factor at the instant of rebound k_{b_r} for different k_ρ. The results show that k_{vp_r} exhibits a non-monotonic dependence on k_ρ, first increasing and then decreasing. At low k_ρ ($k_\rho = 2.5$), the particle experiences substantial fluid drag and interfacial reaction forces, leading to rapid deceleration during penetration and a prolonged travel time before reaching the substrate. Consequently, the rebound kinetic energy reserve is limited, explaining the relatively long detachment time of the PRD mode at this density ratio. Meanwhile, the slower compression process allows the bubble more time for morphological recovery, resulting in a larger shape factor k_{b_r} at rebound and a more flattened configuration. As k_ρ increases, the particle more effectively overcomes fluid resistance, significantly shortening the time to reach the substrate and preserving higher impact momentum, which translates into a stronger rebound velocity. However, with further increase in k_ρ, k_{vp_r} declines again. This indicates that under extremely strong impacts associated with very high k_ρ, a larger fraction of momentum is dissipated through inelastic losses during interfacial penetration and substrate collision. For $k_\rho > 5.24$, both k_{vp_r} and k_{b_r} tend to level off. This behaviour suggests that the mechanical rebound capability approaches a dynamical saturation limit in this parameter range. Owing to the extremely rapid impact process, bubble deformation

https://doi.org/10.1017/jfm.2026.11990 Published online by Cambridge University Press

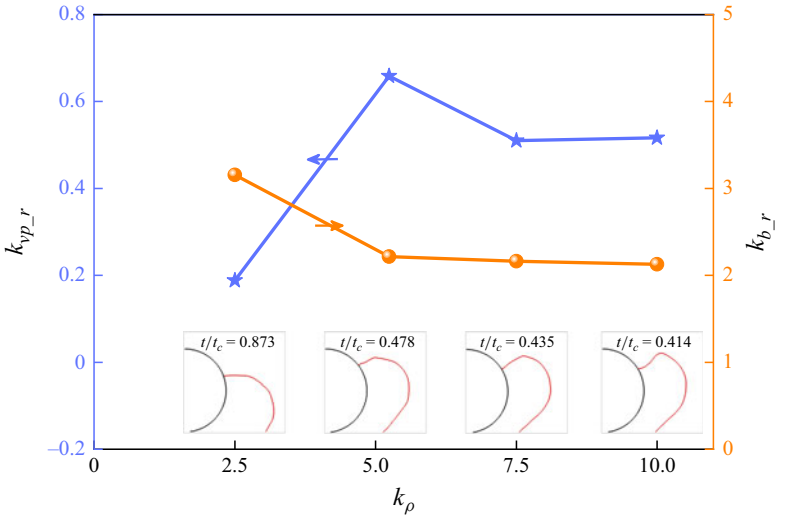


Figure 17. Maximum rebound velocity of the particle and bubble shape factor at different k_ρ.

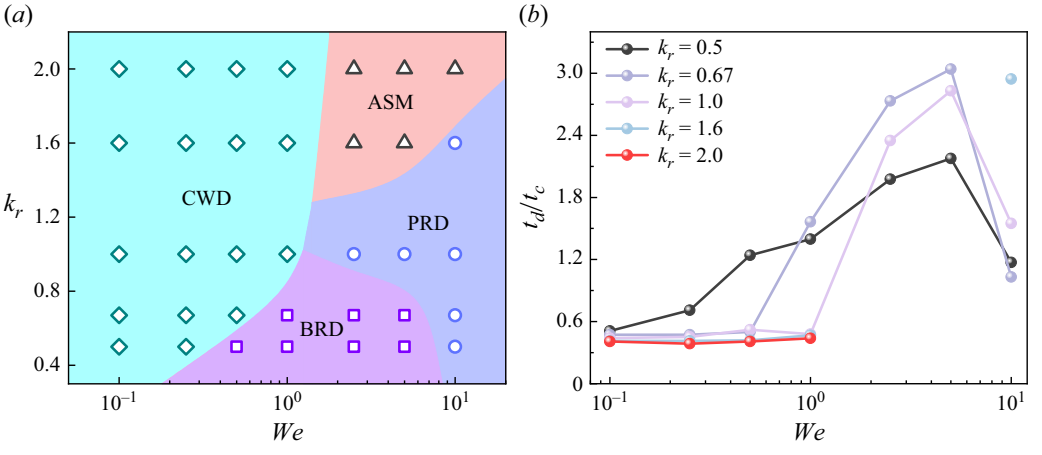


Figure 18. (*a*) Detachment regime map and (*b*) detachment time of the bubble at different Weber numbers and size ratios.

becomes constrained within a restricted dynamical response window and no longer varies significantly with density ratio.

4.6. *Synergistic effects of impact We and particle size ratio*

This section examines the coupled influence of the impact Weber number ($0.1 \leq We \leq 10$) and the particle-to-bubble size ratio ($0.5 \leq k_r \leq 2$). The particle contact angle is fixed at 90°, and the particle–fluid density ratio is $k_\rho = 5.24$. The detachment-mode phase diagram is shown in figure 18(*a*). In the low-inertia regime ($We \leq 1$), the system predominantly exhibits CWD. As k_r increases, the CWD regime expands towards lower We, indicating that larger particles promote capillary-wave-driven detachment under weak-impact conditions. Entering the high-inertia regime ($We \geq 2.5$), the detachment mode switches significantly with increasing k_r. For small size ratios ($k_r < 1$), the system tends to enter the BRD mode. When $k_r = 1$ at sufficiently large We, the system transitions to PRD.

https://doi.org/10.1017/jfm.2026.11990 Published online by Cambridge University Press

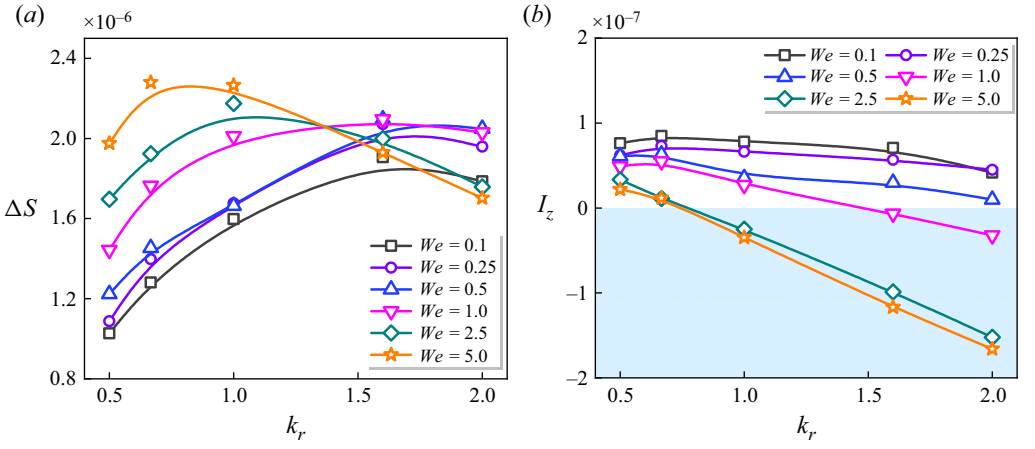


Figure 19. (*a*) Bubble local interfacial area variation and (*b*) vertical impulse at $t/t_c = 0.127$ under different Weber numbers and size ratios.

However, for larger size ratios ($k_r \geq 1.6$), the increased particle mass leads to insufficient bubble rebound energy to overcome inertial suppression, and the system readily falls into the ASM, preventing detachment. Figure 18(*b*) further presents the variation of the dimensionless detachment time t_d/t_c with *We* and k_r. In the CWD regime, detachment time remains relatively short for all size ratios. Once *We* exceeds the mode-transition threshold, t_d/t_c increases sharply. In the BRD regime, the detachment time increases with both k_r and *We*, reflecting enhanced penetration depth and prolonged energy recovery. Upon transition to the PRD regime, t_d/t_c decreases again due to the strong mechanical rebound contribution.

To clarify the mechanism by which k_r regulates detachment-mode transitions, figure 19 extracts the local interfacial area variation ΔS caused by bubble spreading over the particle and the vertical impulse I_z at the end of the first stage ($t/t_c = 0.127$). The results show that ΔS exhibits a non-monotonic dependence on k_r, first increasing and then decreasing. The peak position is strongly influenced by impact inertia: for $We \leq 1.0$, the maximum ΔS occurs near $k_r = 1.6$; for $We > 1.0$, the peak shifts forward to around $k_r = 1.0$. This peak shift reflects the transition from interfacial-dominated to inertia-dominated dynamics. Under weak inertia, larger particle surface area facilitates greater interfacial extension and potential energy accumulation. However, as *We* increases, enhanced inertial compression suppresses interfacial deformation, making smaller size ratios more favourable for reaching deformation saturation.

The vertical impulse I_z decreases monotonically with increasing k_r, and the decline rate intensifies with *We*. At low *We*, all size ratios maintain positive impulse, ensuring the spontaneous driving capability of the CWD mode. As k_r increases, however, inertia-induced compression associated with greater particle mass becomes dominant, driving I_z towards negative values. This effect is particularly pronounced at $We = 5.0$, where the steepest decline of I_z with k_r is observed, highlighting the strong acceleration of downward compression for large particles under high inertia.

Figure 20 further presents the evolution of the bubble detachment capability factor η. The factor decreases continuously with increasing k_r and enters the negative regime at high *We*. From an energy-partition perspective, this explains why large particles tend to trap the system in the ASM due to insufficient upward momentum despite significant interfacial deformation. Overall, the size ratio regulates detachment-mode transitions by

https://doi.org/10.1017/jfm.2026.11990 Published online by Cambridge University Press

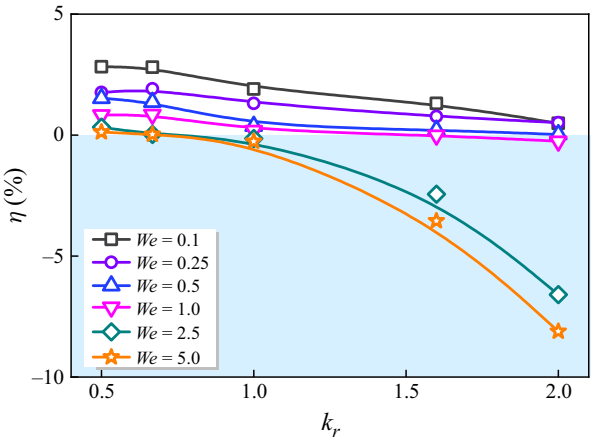


Figure 20. Bubble detachment capability factor η under different We and k_r.

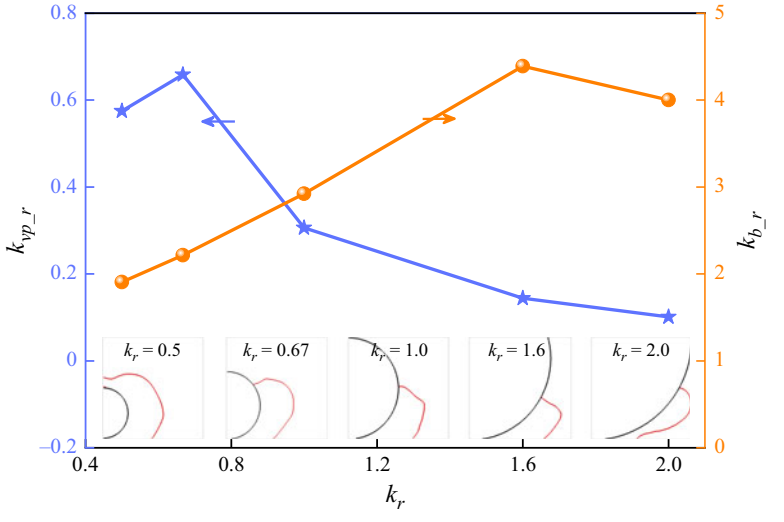


Figure 21. Maximum rebound velocity of the particle and bubble shape factor at different k_r.

modifying the available deformation space and momentum dissipation pathways. When k_r lies within an intermediate range, the system achieves a more favourable balance between deformation energy storage and maintenance of upward vertical momentum, thereby enhancing detachment robustness.

Focusing on the post-transition dynamics in the PRD regime, figure 21 extracts the maximum particle rebound velocity k_{vp_r} and the bubble shape factor at the instant of rebound k_{br} under the condition $We = 10.0$, in order to evaluate the size effect on rebound-stage characteristics. The results show that as the size ratio k_r increases, the maximum rebound velocity k_{vp_r} decreases markedly, while the bubble shape factor k_{br} increases correspondingly. This trend indicates that larger particles experience more severe momentum dissipation during penetration through the bubble and subsequent impact with the substrate. As k_r increases, the reduction in particle velocity prior to substrate collision becomes more pronounced, thereby limiting the rebound velocity achieved during the rebound stage. Meanwhile, the increase in k_{br} with k_r reflects stronger horizontal

https://doi.org/10.1017/jfm.2026.11990 Published online by Cambridge University Press

expansion of the bubble under the compression of larger particles, implying more intense mechanical suppression. Such a strongly compressed state corresponds to greater storage of deformation potential energy. However, under large-size-ratio conditions, the substantial drop in particle rebound velocity k_{vp_r} means that the accumulated mechanical kinetic energy is insufficient to synergistically combine with the stored deformation energy to overcome adhesive resistance. Consequently, when $k_r = 2$, the system transitions into the ASM. In contrast, within the range $k_r < 1.0$, particles possess stronger penetration capability and higher rebound velocities, providing sufficient mechanical compensation to drive bubble detachment. This ensures efficient detachment under high-*We* conditions.

5. Conclusions

An axisymmetric extension of the VOSET-IBM-DEM was developed to investigate bubble detachment from a solid surface induced by particle impact. Three distinct detachment modes were identified: CWD, BRD and PRD. The vertical Kelvin impulse provides a unified framework for interpreting all detachment modes. Bubble detachment is associated with a reversal of the vertical impulse from negative to positive, establishing a net upward momentum. Based on this mechanism, a bubble detachment capability factor η is introduced to characterise the conversion of released energy into upward detachment motion. Mode transitions are governed by the competition between capillary-wave-driven momentum generation and inertia-induced suppression. The CWD regime is generally confined to $We \lesssim 1$, whereas the onset of PRD occurs near $We \approx 10$. The influence of particle properties varies among the three detachment modes. The onset boundary of PRD exhibits only weak sensitivity to particle properties, reflecting the dominance of particle collision, whose associated energy exceeds the released surface energy by one to two orders of magnitude. Within the PRD regime, the rebound velocity exhibits a non-monotonic dependence on density ratio, first increasing and then decreasing, while both the rebound velocity and the bubble deformation factor approach saturation at $k_\rho > 5.24$. The size ratio k_r associated with the maximum surface energy release shifts from $k_r \approx 1.6$ at $We \leq 1$ to $k_r \approx 1.0$ at $We > 1$, indicating a transition from capillary-dominated to inertia-influenced deformation dynamics. These findings establish the detachment capability factor η and the associated regime boundaries as useful criteria for characterising particle-induced bubble detachment.

The present study provides a mechanistic framework for understanding and predicting particle-induced bubble detachment in boiling heat transfer and related gas–liquid–solid multi-phase systems. It should be noted that the present simulations are restricted to axisymmetric configurations and neglect phase change at the vapour–liquid interface. Future work will extend the model to fully three-dimensional boiling systems to investigate the coupled effects of particle motion, bubble growth and phase-change heat transfer under realistic operating conditions.

Supplementary material. Supplementary material is available at https://doi.org/10.1017/jfm.2026.11990.

Acknowledgements. X.C. gratefully acknowledges Professor S. Takagi of the University of Tokyo for valuable discussions and insightful suggestions during the revision of the manuscript.

Declaration of interests. The authors report no conflict of interest.

https://doi.org/10.1017/jfm.2026.11990 Published online by Cambridge University Press

References

Best, J.P. & Blake, J.R. 1994 An estimate of the Kelvin Impulse of a transient cavity. *J. Fluid Mech.* **261**, 75–93.

Brabcová, Z., Karapantsios, T., Kostoglou, M., Basařová, P.M. & Matis, K. 2015 Bubble-particle collision interaction in flotation systems. *Colloids Surf. A Physicochem. Engng Asp.* **473**, 95–103.

Bureš, L.D. & Sato, Y. 2022 Comprehensive simulations of boiling with a resolved microlayer: validation and sensitivity study. *J. Fluid Mech.* **933**, 1–58.

Chen, H., Liu, H.-R., Gao, P. & Ding, H. 2019 Submersion of impacting spheres at low Bond and Weber numbers owing to a confined pool. *J. Fluid Mech.* **884**, A13–7.

Chen, X., Yin, B. & Dong, F. 2024*a* Synergistic effect of ribs and particles on flow and heat transfer in channels using the CFD-DEM-IBM method. *Powder Technol.* **431**, 119082.

Chen, X., Yin, B. & Dong, F. 2024*b* A hybrid method for the direct numerical simulation of phase change heat transfer in fluid–particle systems. *Phys. Fluids.* **36**, 113332.

Chen, X., Yin, B., Zhang, Y., Xin, L., Ni, J. & Dong, F. 2025*a* Numerical simulation of the dynamics of a bubble lying between a free particle and a solid horizontal surface: spreading and detachment. *Appl. Therm. Engng* **279**, 127970.

Chen, X., Zhang, Y., Jia, H., Yin, B., Ni, J., Xin, L. & Dong, F. 2025*b* Heat transfer performance and bubble-particle interaction dynamics in particle-laden pool boiling. *Intl Commun. Heat Mass Transfer* **163**, 108735.

Chen, X., Zhang, Y., Xu, S.& Dong, F. 2023 Bibliometric analysis for research trends and hotspots in heat and mass transfer and its management of proton exchange membrane fuel cells. *Appl. Energy* **333**, 120611.

Chen, Y., Yu, B., Lu, W., Wang, B., Sun, D., Jiao, K., Zhang, W. & Tao, W. 2024 Review on numerical simulation of boiling heat transfer from atomistic to mesoscopic and macroscopic scales. *Intl J. Heat Mass Transfer* **225**, 125396.

Cheng, X., Sun, T.-P. & Gordillo, L. 2021 Drop impact dynamics: impact force and stress distributions. *Annu. Rev. Fluid Mech.* **54**, 57–81.

Deen, N.G., Van Annaland, M.S. & Kuipers, J.A.M. 2009 Direct numerical simulation of complex multi-fluid flows using a combined front tracking and immersed boundary method. *Chem. Engng Sci.* **64**, 2186–2201.

Ding, H., Li, E.Q., Zhang, F.H., Sui, Y., Spelt, P.D.M. & Thoroddsen, S.T. 2012 Propagation of capillary waves and ejection of small droplets in rapid droplet spreading. *J. Fluid Mech.* **697**, 82–114.

Eggers, J., Sprittles, J.E. & Snoeijer, J.H. 2024 Coalescence dynamics. *Annu. Rev. Fluid Mech.* **57**, 61–87.

Fardan, A., Berndt, C.C. & Ahmed, R. 2021 Numerical modelling of particle impact and residual stresses in cold sprayed coatings: a review. *Surf. Coatings Technol.* **409**, 126835.

Ge, Y. & Fan, L.-S. 2007 Droplet-Particle collision mechanics with film-boiling evaporation. *J. Fluid Mech.* **573**, 311–337.

Gong, C., Li, D. & Kang, C. 2022 Visualization of the evolution of bubbles in the spray sheet discharged from the air-induction nozzle. *Pest Manag. Sci.* **78**, 1850–1860.

Han, J., Fang, S., He, X., Wang, L., Li, C., Wu, J., Cai, Y. & Wang, Y. 2022 Combination of aqueous two-phase flotation and inverse transition cycling: strategies for separation and purification of recombinant β-glucosidase from cell lysis solution. *Food Chem.* **373**, 131543.

Hassanzadeh, A., Firouzi, M., Albijanic, B. & Celik, M.S. 2018 A review on determination of particle–bubble encounter using analytical, experimental and numerical methods. *Miner. Engng* **122**, 296–311.

Hirt, C.W. & Nichols, B.D. 1981 Volume of fluid (VOF) method for the dynamics of free boundaries. *J. Comput. Phys.* **39**, 201–225.

Hsu, C.-C., Chiu, Y.-H., Tsai, F.-T., Chou, S.-H., Sheng, L.-T. 2024 The effects of magnetic field control on the aggregation of magnetic particles on the heating surface during pool boiling. *Intl Commun. Heat Mass Transfer* **152**, 107289.

Huang, W., Lori, M.S., Yang, A., Zhuang, K., Cheng, Y., Chen, M., Sun, C., Ming, T., Cui, H. & Cheng, J. 2026 Bubble-burst-induced puddle jumping and jet printing. *Nat. Commun.* **17**, 1818.

Iwata, R., Takeuchi, S. & Kajishima, T. 2010 Large-scale analysis of interactive behaviors of bubbles and particles in a liquid by a coupled immersed boundary and VOF technique. *Multiphase Sci. Technol.* **22**, 233–246.

Janssen, N., Fetzer, J.R., Grewing, J., Burgmann, S. & Janoske, U. 2023 Experimental investigation of particle–droplet–substrate interaction. *Exp. Fluids* **64**, 1–13.

https://doi.org/10.1017/jfm.2026.11990 Published online by Cambridge University Press

KAJISHIMA, T., TAKIGUCHI, S. & HAMASAKI, H. 2001 Turbulence structure of particle-laden flow in a vertical plane channel due to vortex shedding. *Jpn. Soc.* **44** (4), 1734–1741.

KUNKELMANN, C. 2011 Numerical modeling and investigation of boiling phenomena. PhD thesis, Technische Universität Darmstadt, Darmstadt.

LAFAURIE, B., NARDONE, C., SCARDOVELLI, R., ZALESKI, S. & ZANETTI, G. 1994 Modelling merging and fragmentation in multiphase flows with SURFER. *J. Comput. Phys.* **113**, 134–147.

LI, J. & LIN, Z. 2023 A height function based momentum balance model to simulate contact angle dynamics with hysteresis. *Intl J. Numer. Meth. Fluids* **95**, 1–22.

LING, K., LI, Z.-Y. & TAO, W.-Q. 2014 A direct numerical simulation for nucleate boiling by the VOSET method. *Numer. Heat Transf. Part a Appl.* **65**, 949–971.

LIU, F., GHIGLIOTTI, G., FENG, J.J. & CHEN, C.H. 2014 Numerical simulations of self-propelled jumping upon drop coalescence on non-wetting surfaces. *J. Fluid Mech.* **752**, 39–65.

DE MALEPRADE, H., CLANET, C. & QUÉRÉ, D. 2016 Spreading of bubbles after contacting the lower side of an aerophilic slide immersed in water. *Phys. Rev. Lett.* **117**, 1–5.

MITRA, S., DOROODCHI, E., PAREEK, V., JOSHI, J.B. & EVANS, G.M. 2015 Collision behaviour of a smaller particle into a larger stationary droplet. *Adv. Powder Technol.* **26**, 280–295.

MITRA, S., EVANS, G.M., DOROODCHI, E., PAREEK, V. & JOSHI, J.B. 2017 Interactions in droplet and particle system of near unity size ratio. *Chem. Engng Sci.* **170**, 154–175.

MOHAMMADI, M., NAZARI, M., KAYHANI, M.H. & AHMADI, G. 2022 Experimental study and visualization of the particle–Bubble collision process. *J. Appl. Mech. Tech. Phys.* **63**, 903–913.

NAM, Y., KIM, H. & SHIN, S. 2013 Energy and hydrodynamic analyses of coalescence-induced jumping droplets. *Appl. Phys. Lett.* **103**, 161601.

PARK, H., AHMADI, S.F., FOULKES, T.P. & BOREYKO, J.B. 2024 Coalescence-induced jumping bubbles during pool boiling. *Adv. Funct. Mater.* **34**, 1–7.

PAWAR, S.K., HENRIKSON, F., FINOTELLO, G., PADDING, J.T., DEEN, N.G., JONGSMA, A., INNINGS, F. & KUIPERS, J.A.M.H. 2016 An experimental study of droplet-particle collisions. *Powder Technol.* **300**, 157–163.

POPINET, S. 2009 An accurate adaptive solver for surface-tension-driven interfacial flows. *J. Comput. Phys.* **228**, 5838–5866.

POPINET, S. 2018 Numerical models of surface tension. *Annu. Rev. Fluid Mech.* **50**, 49–75.

RAHMATI, P., EBRAHIMI-DEHSHALI, M. & HAKKAKI-FARD, A. 2020 Enhancement of pool boiling heat transfer using ferromagnetic beads in a variable magnetic field. *Appl. Therm. Engng* **164**, 114439.

SHI, C., *et al.* 2015 Interaction between air bubbles and superhydrophobic surfaces in aqueous solutions. *Langmuir* **31**, 7317–7327.

SIEGEL, R. & KESHOCK, E.G. 1964 Effects of reduced gravity on nucleate boiling bubble dynamics in saturated water. *AIChE J.* **10**, 509–517.

SINGH, P. & JOSEPH, D.D. 2005 Fluid dynamics of floating particles. *J. Fluid Mech.* **530**, 31–80.

SUN, D.L., QU, Z.G., HE, Y.L. & TAO, W.Q. 2008*a* An efficient segregated algorithm for incompressible fluid flow and heat transfer problems – IDEAL (Inner Doubly Iterative Efficient Algorithm for Linked Equations) part I: mathematical formulation and solution procedure. *Numer. Heat Transf. Part B Fundam.* **53**, 1–17.

SUN, D.L., QU, Z.G., HE, Y.L. & TAO, W.Q. 2008*b* An efficient segregated algorithm for incompressible fluid flow and heat transfer problems – IDEAL (Inner Doubly Iterative Efficient Algorithm for Linked Equations) part II: application examples. *Numer. Heat Transf. Part B Fundam.* **53**, 18–38.

SUN, D.L. & TAO, W.Q. 2010 A coupled volume-of-fluid and level set (VOSET) method for computing incompressible two-phase flows. *Intl J. Heat Mass Transfer* **53**, 645–655.

SUN, X. & SAKAI, M. 2016 Direct numerical simulation of gas–solid–liquid flows with capillary effects: an application to liquid bridge forces between spherical particles. *Phys. Rev. E* **94**, 1–22.

SUSSMAN, M. 2001 An adaptive mesh algorithm for free surface flows in general geometries. In *Adaptive Method of Lines* (ed. A. Vande Wouver, P. Saucez & W.E. Schiesser), pp. 207–231. Chapman and Hall/CRC.

SUSSMAN, M., ALMGREN, A.S., BELL, J.B., COLELLA, P., HOWELL, L.H. & WELCOME, M. 1996 An adaptive level set approach for incompressible two-phase flows. *Am. Soc. Mech. Engng Fluids Engng Div. FED* **238**, 355–360.

TSUJI, Y., KAWAGUCHI, T. & TANAKA, T. 1993 Discrete particle simulation of two-dimensional fluidized bed. *Powder Technol.* **77**, 79–87.

WANG, J., HUANG, W., YAO, N., YANG, C., CHEN, S. & WANG, G. 2025 Force analysis of bubble-particle detachment colliding with a solid surface. *Powder Technol.* **451**, 120454.

https://doi.org/10.1017/jfm.2026.11990 Published online by Cambridge University Press

WANG, X., WU, G., ZHENG, X., DU, X. & ZHANG, Y. 2022 Theoretical investigation and experimental support for the cavitation bubble dynamics near a spherical particle based on Weiss theorem and Kelvin impulse. *Ultrason. Sonochem.* **89**, 106130.

WASHINO, K., CHAN, E.L., TSUJIMOTO, T., TSUJI, T. & TANAKA, T. 2023 Development of resolved CFD–DEM coupling model for three-phase flows with non-spherical particles. *Chem. Engng Sci.* **267**, 118335.

WU, G., CHEN, S., DU, W., ZHAI, S., ZENG, S., YU, Y. & ZHOU, W. 2022 Simulation on a three-dimensional collision of a moving droplet against a moving super-hydrophobic particle. *Powder Technol.* **405**, 117558.

YANG, G., ZHANG, W., BINAMA, M., LI, Q. & CAI, W. 2023 Review on bubble dynamic of subcooled flow boiling-part B: behavior and models. *Intl J. Therm. Sci.* **184**, 108026.

YOON, I. & SHIN, S. 2021 Computational study on dynamic behavior during droplet-particle interaction. *Chem. Engng Sci.* **241**, 116656.

YU, H., YANG, S. & WANG, H. 2024 VOF-DEM numerical study of mesoscale bubble dynamics in the gas-liquid-solid three-phase flow system. *AIChE J.* **70**, e18614.

YUKI, Y., TAKEUCHI, S. & KAJISHIMA, T. 2007 Efficient immersed boundary method for strong interaction problem of arbitrary shape object with the self-induced flow. *J. Fluid Sci. Technol* **2**, 1–11.

ZHANG, Z.-H., WANG, S., CHENG, L., MA, H., GAO, X., BRENNAN, C.S. & YAN, J.-K. 2023 Micro-nano-bubble technology and its applications in food industry: a critical review. *Food Rev. Intl* **39**, 4213–4235.

https://doi.org/10.1017/jfm.2026.11990 Published online by Cambridge University Press